Unsteady characteristics of inlet vortices

Z. Wang[1] and I. Gursul[2]

University of Bath, Bath, United Kingdom

Abstract

An experimental study of the unsteady characteristics of inlet vortices has been conducted using a high-frame-rate digital particle image velocimetry (DPIV) system. The results revealed the formation of a pair of counter rotating inlet vortices for the no-wind configuration and one single inlet vortex when there was crosswind. In all measurement planes, from near the ground to the inlet, evidence of vortex meandering with quasi-periodicity was found. The vortex meander is dominant in the direction of the crosswind and its amplitude increases with crosswind velocity. The proper orthogonal decomposition (POD) analysis of the instantaneous velocity field suggested that the most energetic mode was a helical displacement wave, corresponding to the first helical mode. Similarities with the meandering of the trailing vortices from wings were noted. The present results also suggest that the unsteady characteristics of the focus of separation formed on the ground might be responsible for the unsteady nature of the inlet vortex.

Nomenclature

a_M	=	Meandering amplitude of inlet vortex (mm)
D_i	=	Inlet diameter (mm)
D_0	=	Outer diameter of the inlet tube (mm)
E	=	Spectral density (dB/Hz)

[1] Lecturer, Department of Mechanical Engineering.
[2] Professor, Department of Mechanical Engineering, i.a.gursul@bath.ac.uk

f	=	Frequency (Hz)
H	=	Inlet height (mm)
N	=	Number of snapshots of the inlet vortex
P	=	Probability of instantaneous inlet vortex locations (%)
Q	=	The inlet volumetric flow rate (LPM)
r_i	=	Radius of the instantaneous inlet vortex (mm)
r_{oi}	=	$\Sigma\, r_i/N$, Conditionally-averaged radius of the instantaneous inlet vortex (mm)
r_o	=	Radius of the time-averaged inlet vortex (mm)
t	=	Time (s)
U_i	=	Inlet velocity (m/s)
U_∞	=	Crosswind velocity (m/s)
x	=	Coordinate in the direction of the crosswind
x_c	=	Coordinate of the location of the time averaged inlet vortex in the direction of the crosswind (mm)
x_i	=	Coordinate of the location of the instantaneous inlet vortex in the direction of the crosswind (mm)
y	=	Coordinate in the direction perpendicular to the crosswind
y_c	=	Coordinate of the location of the time averaged inlet vortex in the direction perpendicular to the crosswind (mm)
y_i	=	Coordinate of the location of the instantaneous inlet vortex in the direction perpendicular to the crosswind (mm)
z	=	Vertical coordinate
Γ	=	Circulation (m^2/s)
ω_y	=	Vorticity in the vertical plane perpendicular to the axis of the inlet model (s^{-1})
ω_z	=	Vorticity in the horizontal planes parallel to the ground (s^{-1})

1. Introduction

Inlet vortices (or ground vortices), formed between engine and ground, have been a problem for aeroplanes operating on the ground (e.g., Colehour and Farquhar 1971; de Siervi et al. 1982; Gajewski 1988; Johns 2002; Shmilovich and Yadlin 2006). These 'tornado' like vortical flows may kick up debris from the ground, which can be ingested by engines and result in engine damage. The inlet vortices can also entrain dust into engine compressors, and as a result, erode blades and further degrade turbine performance and cause a reduction in engine life (Colehour and Farquhar 1971). Furthermore, the inlet vortices may also cause a distortion of the inlet flow that affects engine performance such as reduced engine efficiency or engine surge (Nakayama and Jones 1999; Johns 2002; Shmilovich and Yadlin 2006). As a result, there has been a great interest in understanding the characteristics of inlet vortices in the past decades.

The mechanisms of inlet vortex formation have been a popular subject of research since the 1950s (Rodert and Garrett 1955; Klein 1959; Trapp and Girardi 2010). Colehour and Farquhar (1971) employed potential flow analysis to study the conditions necessary for the existence of an inlet vortex. Their investigation suggested that the existence of a stagnation point on the ground is a vital criterion for the inlet vortex formation. De Siervi et al. (1982) suggested that there might be two different mechanisms of inlet vortex generation. The first of these is the amplification of ambient vorticity as the vortex lines are stretched and drawn into the inlet under headwind conditions (see also Shin et al. 1986a). The second mechanism proposed by de Siervi et al. (1982) is that inlet vortex can arise in an (upstream) irrotational flow, for an inlet in crosswind, which does not require the presence of ambient vorticity. The vorticity source in this case is the boundary layer on the inlet external surface. These authors demonstrated that twin inlets without any ground plane can exhibit inlet vortex. In the presence of a ground plane, boundary layer forms and the first mechanism can also

contribute for cross-wind conditions. Most recently, Brix et al. (2000)'s experiments suggested that even without an ambient flow an inlet vortex would form. Murphy et al. (2010) proposed that, under quiescent condition, the source of vorticity is the boundary layer which is generated by the interaction of the intake-induced flow and the ground surface.

Previous investigations have greatly improved our understanding of the inlet vortex phenomenon. The existence of a stagnation point on the ground is essential for the phenomenon to appear (Colehour and Farquhar 1971; Nakayama and Jones 1999, Funk et al. 2001); the parameters that can be used to characterize this phenomenon are the ratio U_∞/U_i of ambient velocity to inlet velocity, the ratio H/D_i of inlet height to inlet diameter, the wind direction, and the ratio of U_i to the product of upstream wind velocity gradient and D_i (de Siervi et al. 1982; Shin et al. 1986a; Nakayama and Jones 1999). It has been found that increasing U_i/U_∞ or decreasing H/D_i can either increase the tendency for a vortex to form or strengthen the existing vortex (de Siervi et al. 1982).

Unsteady characteristics of the inlet vortices have not received much attention. Brix et al. (2000) observed unsteadiness in their hot-wire measurements. Funk et al. (2001) noted unsteadiness in flow visualization and PIV measurements of the inlet vortices, however these were not quantified. Karlsson and Fuchs (2000) performed Large Eddy Simulations of the unsteady characteristics of vortex systems between the engine inlet and the ground under headwind condition. Their results suggested that the velocity components between inlet and ground may have different modes with dominant frequencies on the order of $St = fD_i/U_i = O(10^{-3})$ to $O(10^{-2})$. Secareanu et al. (2005)'s LDA measurements of the axial velocity component of the inlet vortex, formed between the engine inlet and the ground under headwind condition, exhibited large coherent fluctuations with a dominant frequency of $St = fD_i/U_i = 0.06$. More recently, Murphy and MacManus (2011a, 2011b) conducted PIV

measurements (at a low frame rate of 7.5 Hz) and observed variations of the vortex core radius as a function of time.

Such variation of the vortex core radius is typical of vortex *meandering* (or *wandering*), which was observed in a variety of vortical flows, including tip vortices from high aspect ratio wings (Corsiglia et al. 1973; Baker et al. 1974; Green and Acosta 1991; Devenport et al. 1996; Roy and Leweke 2008; del Pino et al. 2011) and from aircraft models (Jacquin et al. 2001; Jacquin et al. 2003), leading-edge vortices over delta wings (Menke and Gursul 1997; Gursul and Xie 2000) and low aspect ratio fins (Beresh et al 2010). While some studies found vortex meandering to be broadband (Baker et al. 1974; Green and Acosta 1991; Devenport et al. 1996), others showed the existence of dominant peaks in the spectra (Jacquin et al. 2001, 2003; Roy and Leweke 2008; del Pino et al. 2011). Various mechanisms were suggested, including free stream turbulence, propagation of instabilities that develop during the roll-up of the vortex ("source perturbations"), and long-wavelength and short-wavelength instabilities (Jacquin et al. 2001, 2003). There is clear evidence that turbulence outside of the vortex can increase the meandering amplitude (Bailey et al. 2006; Margaris et al. 2008) by interacting with the vortex. There is also supporting evidence that instabilities from the roll-up process can cause meandering (Gursul and Xie 2000). Hence there may be a combination of different mechanisms. There are no systematic time-resolved studies on the meandering of the inlet vortices.

This paper presents an experimental investigation of the unsteady characteristics of inlet vortices using a high-frame-rate digital particle image velocimetry (PIV) system. The objective of this study is to document the meandering of the inlet vortices as a function of the crosswind velocity. Various statistical measures were used to study the motion of the vortex cores. The proper orthogonal decomposition analysis of the measured velocity field was also performed to understand the nature of the vortex unsteadiness.

2. Experimental Apparatus and Methods

2.1. Model

The experiments were carried out in a low-speed, closed-loop open-jet wind tunnel with a circular working section of 760 mm in diameter, located in the Department of Mechanical Engineering, University of Bath. The tunnel has a maximum speed of 30 m/s and a freestream turbulence level of 0.1%. The inlet model was made of polyvinyl chloride (PVC) with an internal diameter of D_i = 51 mm, a wall thickness of 2 mm and a round (semi-circular) edge profile. The schematic of the experimental arrangement is shown in Figure 1. The inlet model was mounted over a flat ground plate of 345 mm by 345 mm located approximately in the middle of the working section. The plate has a streamlined leading edge shape (5:1 elliptical) which prevents possible flow separation. We have no reason to suspect any leading-edge separation for this flat plate, which was used in a previous investigation by Williams (2009). The resulting boundary layer was laminar as expected, and no tripping was used in the present study. The model was placed perpendicular to the tunnel flow, with an inlet height to diameter ratio of H/D_i = 0.75. A Numatic WVD900-2 vacuum cleaner was used to produce a constant inlet velocity of U_i = 30 m/s which corresponds to a volumetric flow rate of Q = 3677 LPM. The inlet volumetric flow rate was directly measured using a Trogflux F VA Rotameter. For all the measurements (different ingestion cases), the inlet volumetric flow rate was maintained constant at Q = 3677 LPM (U_i = 30 m/s) by a regulator valve.

2.2. Velocity measurements

The flow was seeded with oil droplets produced by a TSI model 9307-6 multi-jet atomizer. The atomizer worked best using olive oil and the mean size of the droplets was 1 μm. Figure 2 shows the measurement planes and camera arrangement for the PIV

measurements. Time-accurate flow measurements were conducted in the vertical plane ($y = -0.03D_i$), which is parallel and 1.5 mm ($0.03D_i$) away from the inlet, the horizontal plane ($z = -0.57D_i$), underneath the inlet (9 mm, or $0.18D_i$, away from the ground) and close to the ground plate (at $z = -0.73D_i$), (1 mm, or $0.02D_i$, away from the surface) using a high-frame-rate Digital Particle Image Velocimetry (DPIV) system (Figure 2). Illumination of the desired planes was achieved using a New Wave Pegasus Nd:YLF double pulse high speed laser with a maximum energy of 10 mJ per pulse. The images were captured using a TSI PowerView HS-3000 high-speed complementary metal-oxide-semiconductor (CMOS) camera with a resolution of 1024 × 1024 pixels. The camera lens was Nikon 60mm f/2.8D AF Micro NIKKOR. A TSI LaserPulse synchroniser unit was utilized to link the camera and the laser to enable accurate capture of two frames for cross-correlation analysis. The system was operated at 3.0 kHz, giving the capture of velocity field at 1.5 kHz. Approximately 6000 instantaneous images were captured for each of the measurement planes. The commercial software TSI Insight3G and a fast Fourier transform (FFT) cross-correlation algorithm were used for the analysis of the results obtained. An interrogation window size of 24 × 24 pixels was used to produce velocity vectors for further processing. The effective grid size varied from 1.20 to 1.54 mm in these measurements. Experiments were conducted at crosswind velocities of $U_\infty/U_i = 0$ (no-wind), 0.1, 0.16, 0.19 and 0.25, respectively. The typical run time for each measurement was 2 seconds.

2.3. Uncertainties

Attempts have been made to evaluate and address the main sources of uncertainty. The methods used for estimating uncertainty are those outlined by Moffat (1982). For all

uncertainty estimations, errors due to the digitisation of a measured signal by data acquisition hardware were not considered significant.

The uncertainties of inlet velocity U_i and crosswind velocity (tunnel velocity) U_∞ were estimated as ±2.5%. The dimensions of the inlet model and ground plate were found as ± 0.2 mm (0.4%D_i). The non-dimensional inlet model height H/D_i was estimated with an uncertainty of ±1.5%. For PIV measurements, the uncertainty of aligning laser sheets was estimated as ±0.5 mm (1%D_i). A main source of PIV error for the particular 2D PIV system used for these measurements is due to out-of-plane motion of the seeding particles (perspective error). We estimate a maximum velocity error of ±2.5% of the free stream velocity. Given that these errors occur at the extremities of the field of view, and the area of interest of the measurements is much closer to the centre of the field of view, an error of ±1.5% was considered a more appropriate figure. Another source of uncertainty for PIV measurements is that user error can be significant, including the level of seeding, misalignment of the PIV setup, combinations of parameters used to analyse the images, etc. Taken all these aspects into consideration, the measurement uncertainties for velocity and vorticity were estimated as ±2% and ±4%, respectively. The accuracy of identifying the vortex core position and vortex radius was estimated as half of the effective grid size of PIV measurements, which varied from 0.6 to 0.77 mm (1.2%-1.5%D_i).

3. Results and Discussion

3.1. Time-averaged inlet vortices

The time-averaged vorticity fields superposed with the velocity vectors in the vertical plane at the inlet entrance are presented in Figure 3. It can be observed that, when there was no wind (Fig. 3a), a pair of counter rotating inlet vortices was formed at the lower part of the

inlet. The strength of the vortex pair was however relatively weak compared to the other cases with crosswind. Note that Figure 3a has different contour levels. Brix et al. (2000) inferred from their hot-wire measurements that the formation of a concentrated counter-rotating inlet vortex pair is possible when there is no ambient flow or a symmetric head wind. Such vortex pairs were also observed by Murphy and MacManus (2011b) in their PIV measurements for quiescent conditions and for headwind. The present investigation clearly captures this inlet vortex pair without ambient flow.

When there was a crosswind of U_∞ / U_i = 0.1 (Fig. 3b), the inlet vortex pair disappeared and only one stronger anti-clockwise vortex was formed at the lower part of the inlet. When the crosswind velocity was increased to U_∞ / U_i = 0.16 (Fig. 3c), it was observed that the time-averaged inlet vortex moved downstream in the crosswind direction and towards the trailing edge of the inlet model, and also appeared to be weaker. With further increase in the crosswind velocity to U_∞ / U_i = 0.19, no inlet vortex was observed at the inlet entrance (Fig. 3d). This will be clarified further below.

The time-averaged vorticity fields measured in the horizontal planes underneath the inlet and near the ground plane surface at various crosswind velocities are presented in Figures 4 and 5, respectively. Figures 4 and 5 confirm that the inlet vortices observed in the present investigation were originated from the separation points formed on the ground. In each case, the vortices observed at the inlet entrance were also seen in the other measurement planes, giving a picture of the three-dimensional vortex trajectory. For the particular case of the largest crosswind velocity of U_∞ / U_i = 0.19, the vortex was not seen in the inlet (Fig. 3d), although it was possible to identify it just outside of the inlet (Fig. 4d) and also near the ground (Fig. 5d). In this case, a ground vortex is also formed on the ground surface as in

other cases. However, the 'tornado' like vortex bends around the inlet due to the relatively strong crosswind (Fig. 4d). As a result, no vortex was observed at the inlet entrance (Fig. 3d).

The sketch in Figure 6 shows that at $U_\infty/U_i = 0.19$, the tornado like vortex formed on the ground failed to enter the inlet due to strong crosswind. In this scaled drawing, the locations of the vortex near the ground, between the inlet and ground, and at the entrance to the inlet were denoted by solid circles. To the best of our knowledge, this is the first study to report such vortex topology.

Previous data in the literature show that when the crosswind velocity is above a critical value no vortex is found at the inlet. This critical boundary is somewhat larger according to the data in Shin et al. (1986b) ($U_\infty/U_i = 0.28$ for our height-to-diameter ratio, however very thick boundary layers exist and Reynolds number is also one order of magnitude larger for their data set). Apparently, the critical crosswind velocity for the border between the vortex and no-vortex regimes, is smaller in our case.

Figure 7 presents the time-averaged streamline patterns near the ground plate surface at various crosswind velocities. In Figure 7, time-averaged streamlines near the surface are spiralling into singular points; hence they are foci of separation. For zero crosswind, there are two such points corresponding to the pair of vortices. For all other cases, one focus of separation is observed. As the crosswind velocity was increased to $U_\infty/U_i = 0.25$, no focus of separation was observed on the ground plane surface (not shown), therefore, the 'tornado' like vortical structure failed to form.

It has been found that decreasing U_∞/U_i or H/D_i can either increase the tendency for a vortex to form or strengthen the existing vortex (de Siervi et al. 1982). When the crosswind velocity is above a critical value no vortex was found at the inlet. There are many studies of

the headwind conditions to establish vortex/no-vortex boundary, but not many for the case of the crosswind conditions. The only available substantial data set were presented by Shin et al. (1986b), although the conditions are not exactly the same (thick shear flows were generated near the ground surface). The critical boundary is somewhat larger according to the data in Shin et al. (1986b) (U_∞/U_i = 0.28). When we increased crosswind velocity to U_∞/U_i = 0.25, a blow-away condition was reached, as a result, the 'tornado' like vortical structure failed to form.

3.2. Inlet vortex meandering

Previous investigations suggested that inlet vortex is highly unsteady (Brix et al. 2000; Funk et al. 2001; Secareanu et al. 2005; Murphy and MacManus 2011a, 2011b). The present time-accurate PIV measurements at the inlet entrance indicate that the inlet vortex was meandering. Figure 8 presents the instantaneous location of the inlet vortex in the vertical plane (y = –0.03D_i) near the inlet. The dots represent the vortex centres obtained from the analysis of velocity fields. The vortex centre was defined as the location of zero velocity magnitude in the PIV measurement plane and rounded to the nearest grid point, giving an accuracy of half of the effective grid size, which varies from 0.6 to 0.77mm (1.2%-1.5%D_i). (Spacing of the dots indicates the spatial resolution of the measurements). Colours represent the probability of the inlet vortex at each grid point. It can be observed that without crosswind (U_∞/U_i = 0) both vortices were meandering around within a relatively small area around the time-averaged location (the black symbol in Fig. 8). When there was a crosswind of U_∞/U_i = 0.1, only the anti-clockwise vortex (Fig. 3b) was observed moving around at the lower part of the inlet (Fig. 8b). Further increasing the crosswind velocity to U_∞/U_i = 0.16 (Fig. 8c), the instantaneous locations of inlet vortex varied in a larger area, suggesting an

increased magnitude of unsteadiness. Note that, for all the crosswind velocities tested, the area in which the vortices were meandering exhibits a nearly elliptical shape. The elliptical shape suggests that vortex meandering is dominant in one direction.

The instantaneous locations of inlet vortex in the horizontal plane underneath the inlet and near the ground plane surface are presented in Figures 9 and 10, respectively. (In these figures, the case of U_∞/U_i = 0 was not included as the PIV camera view was partially obstructed by the inlet pipe as seen in Figures 4 and 5). For U_∞/U_i = 0.1 and 0.16, the distribution of instantaneous locations of the inlet vortex in the horizontal plane underneath the inlet (Figs. 9a & b) and near the ground plane surface (Figs. 10a & b) are similar to those at the inlet entrance (Figs. 8b & c), i.e., the elliptical area in which the vortices were meandering and the larger area of meander with increasing crosswind velocity. Similar observation can be made at U_∞/U_i = 0.19 as well (Figs. 9c and 10c) though the 'tornado' like vortex did not enter the inlet due to the relatively stronger crosswind (Fig. 6). The meandering amplitude is larger in the crosswind direction than in the direction perpendicular to it.

In order to quantify the inlet vortex meandering, Figure 11 presents the standard deviation (*SD*) of the coordinates of inlet vortex location (Fig. 11a) and the inlet vortex meandering amplitude (a_M) as a function of crosswind velocity (Fig. 11b). The inlet vortex meandering amplitude is defined as $a_M = \sqrt{\frac{\sum (x_i - x_c)^2 + (y_i - y_c)^2}{N}}$, where N is the number of snapshots of inlet vortex, x_i and x_c are the coordinates of instantaneous and time averaged inlet vortex locations in the direction of the crosswind, y_i and y_c are the coordinates of instantaneous and time averaged inlet vortex locations in the perpendicular direction to the crosswind. Both *SD* and a_M are normalized by the diameter of the inlet tube in Fig. 11. It can be observed that, as expected, both *SD* and a_M increase with increasing crosswind velocity.

Furthermore, for all crosswind velocities tested, Figure 11a suggests that the standard deviation of the coordinates of inlet vortex location in the crosswind direction is roughly twice of that in the perpendicular direction to the crosswind, suggesting that the inlet vortex meander is dominant in the crosswind direction. Note that, variations of SD and a_M exhibit similar trends and magnitudes in the vertical plane at the inlet entrance and the horizontal planes underneath the inlet and near the ground plane surface. Hence, in all planes the meandering has common features. The meandering is more significant in the crosswind direction. The amplitude of the meandering is roughly constant from the ground to the inlet entrance. Also, the meandering amplitude increases substantially with increasing crosswind velocity.

Figure 12 shows the tangential velocity profiles for a snapshot of the vortex and time-averaged vortex in the horizontal plane underneath the inlet at $U_\infty/U_i = 0.16$. It can be seen that the velocity profiles are fairly symmetric about the vortex centre. The radius r_i and r_o were defined as half the distance between the maximum tangential velocities along the velocity profiles for individual snapshots and the time-averaged vortex, respectively. Note that in all cases instantaneous vortex was approximately symmetric, but the time-averaged vortex was highly asymmetric in some cases due to the dominant meandering in one direction. In these cases, an average value of vortex radius was calculated from the maximum and minimum radius. The variation of the conditionally-averaged radius r_{oi}/D_i of the instantaneous inlet vortex with crosswind velocity is presented in Figure 13. It can be observed that, when there was no wind ($U_\infty/U_i = 0$), r_{oi} was relatively small. When there was a crosswind of $U_\infty/U_i = 0.1$, the conditionally-averaged vortex radius r_{oi} increased. With further increase in the crosswind velocity to $U_\infty/U_i = 0.16$ and 0.19, the conditionally-averaged vortex radius r_{oi} decreased slightly. The amplitude of the inlet vortex meandering a_M was normalized by the conditionally-averaged radius of the instantaneous vortex (a_M/r_{oi}),

and is presented in Figure 14. Since the values of crosswind velocity have relatively small effect on r_{oi} (Fig. 13), a_M/r_{oi} exhibits essentially similar trends to those normalized by the inlet diameter D_i (Fig. 11b). For example, a_M/r_{oi} increases with crosswind velocity with the maximum of $a_M/r_{oi} \approx 2$ being observed at $U_\infty/U_i = 0.19$. Note that the amplitude of meandering is around 50% of the radius of the time-averaged vortex for zero crosswind velocity, and can reach around 100% of the radius of the time-averaged vortex. As a comparison with the trailing vortices behind wings, Devenport et al. (1996) reports that the amplitude of the meandering is 30% of the time-averaged core radius.

3.3. Quasi-periodic nature of meandering

The time histories of the coordinates of inlet vortex location in the crosswind direction in the vertical plane at the inlet entrance and the horizontal plane near the ground plate surface at $U_\infty/U_i = 0.16$ are presented in Figure 15. It can be observed that Figs. 15a and 15b exhibit similar trends. For example, the amplitude of x_i/D_i at the inlet entrance (Fig. 15a) and near ground surface (Fig. 15b) exhibit comparable magnitudes of fluctuations and both exhibit quasi-periodic nature. The frequency spectrum calculated from the aforementioned time histories of x_i/D_i are presented in Figure 16. For each measurement, the time history of the coordinate x_i of instantaneous inlet vortex location in the crosswind direction has 3000 samples in 2 seconds (f_{sample}=1500 Hz). We performed FFT analysis with zero-padding on the time series using Hanning window function. The window size was 1024 samples (682.67 ms) and the spectrum was averaged over 3 windows. The resulting frequency resolution was 1.46 Hz ($fD_i/U_i = 0.0025$). It can be observed that the dominant frequency of inlet vortex meander was around $fD_i/U_i \approx 0.005$ in both the vertical plane at the inlet entrance (Fig. 16a) and the horizontal plane near the ground plate surface (Fig. 16b).

With further increase in the crosswind velocity to U_∞/U_i = 0.19, the time history of the coordinates of inlet vortex location in the crosswind direction in the horizontal plane underneath the inlet (Fig. 17a) exhibits similar trend to that near the ground plate surface (Fig. 17b) in terms of the amplitude of fluctuations and the quasi-periodic nature. Note that, at U_∞/U_i = 0.19, the 'tornado' like vortex did not enter the inlet due to the relatively stronger crosswind (Fig. 6). The corresponding frequency spectra of the coordinates x_i/D_i of the inlet vortex location in the crosswind direction are presented in Figure 18. It is seen that the dominant peak is around $fD_i/U_i \approx 0.03$. In summary, dominant peaks on the order of $fD_i/U_i = O(10^{-3})$ to $O(10^{-2})$ have been observed for a range of crosswind velocities. This observation is consistent with Karlsson and Fuchs (2000) and Secareanu et al. (2005)'s studies. Karlsson and Fuchs (2000) studied the unsteady characteristics of vortex systems between the engine inlet and the ground under headwind condition. Their results suggested that the velocity components between inlet and ground may have different mode with dominant frequencies in the same range as our observations. Secareanu et al. (2005)'s LDA measurements of the axial velocity component of the inlet vortex, formed between the engine inlet and the ground under headwind condition, exhibited large coherent fluctuations with dominant frequency of $St = fD_i/U_i = 0.06$.

The quasi-periodic nature of the vortex meandering was reported for trailing vortices behind wings (Jacquin et al. 2003; Bailey and Tavoularis 2008; Roy and Leweke 2008; del Pino et al. 2011). While some investigators (Bailey and Tavoularis 2008; Roy and Leweke 2008) found the wavelength of the meandering is two orders of magnitude greater than the vortex core radius ($\lambda/r_o = O(10^2)$), some others (del Pino et al. 2011) estimated the ratio of the wavelength to the core radius as $\lambda/r_o = O(10^3)$. For inlet vortices, the characteristic wavelength of the meandering can be estimated from the characteristic frequency. As the convection velocity U_C will be order of the inlet velocity U_i at the inlet entrance, we estimate

that the normalized axial wavenumber $kr_o = 2\pi r_o / \lambda = 2\pi r_o f / U_C \approx 0.003$, hence $\lambda / r_o \approx 2\text{x}10^3$. Therefore, the meandering occurs at very large wavelengths with regard to the vortex radius. Such long-wave displacements of vortices were explained by the transient growth of external perturbations (Antkowiak and Brancher 2004). This was demonstrated by the temporal evolution of disturbances in the Lamb-Oseen vortex without axial flow. It was shown that intense amplification of the perturbations of the azimuthal wavenumber $m = 1$ occurs. It was also suggested that substantial transient growth occurs at very large wavelengths (as $kr_o \rightarrow 0$), which is consistent with our observations. The paper by Antkowiak and Brancher (2004) shows that axial flow is not a necessary ingredient for the intense amplification of the spiral mode. In fact this theoretical model has been used as an explanation of the vortex meandering in aircraft vortex wakes. The effects of axial velocity and swirl ratio on vortex meandering should be investigated in future studies.

We also considered whether the vortex shedding from the outer surface of the inlet tube in the crosswind can cause the vortex meandering. We plotted the spectral density E_x of the coordinates x_i of the inlet vortex location as a function of frequency normalized by the outer diameter of the tube D_o and crosswind velocity U_∞ in Figure 19 for the three measurement planes. Although there is some energy around the expected vortex shedding frequency ($fD_o/U_\infty \approx 0.2$), the dominant peaks were located at lower frequencies in most cases. In fact, in the measurement plane near the inlet entrance (closest measurement plane to the vortex shedding), there is less evidence of vortex shedding frequency (Figure 19a). Also, theoretically, we do not expect perturbations to propagate upstream to the ground plane for this kind of vortex flows with jet-like axial velocity. Although we do not have measurements of the axial velocity in our case, jet-like vortices in other vortex flows have been found to be *supercritical*, which means that disturbances can only travel along the axis of the vortex in the downstream direction (Tsai and Widnall, 1980; Leibovich, 1984).

We propose that the case of meandering of the inlet vortex is similar to the case of meandering of trailing vortices behind wings, where perturbations from the vortex roll-up process may cause meandering. The origin of the inlet vortex is the separation on the ground. Hence, it is more likely that the perturbations originate from the ground. In order to support this hypothesis, the variation of the circulation Γ/U_iD_i of the instantaneous inlet vortex near the ground plate surface at $U_\infty/U_i = 0.19$ is shown in Figure 20a. For each instantaneous inlet vortex, the circulation was calculated in a fixed rectangular area enclosing the vortex ($-0.848 \leq x/D_i \leq 0.095$ and $-0.715 \leq y/D_i \leq -0.077$ in Fig. 5d) by performing a surface integral of the vorticity. The selected calculation area was large enough to enclose the area in which the vortex was meandering (Fig. 10c). A line-integral method has also been used, for which a good agreement with the surface integral method was obtained. The results presented in this study are of the surface integral method. The circulation exhibits similar quasi-periodic nature to that of the time histories of the coordinates of the inlet vortex location in the crosswind direction (Fig. 17b). The corresponding frequency spectrum E_Γ of the circulation Γ / U_iD_i of the instantaneous inlet vortex is presented in Figure 20b. It can be seen that the dominant peak of E_Γ is around $fD_i/U_i \approx 0.025$, which is consistent with that observed in the frequency spectrum E_X of the coordinates x_i/D_i of the inlet vortex location in the crosswind direction at $U_\infty/U_i = 0.19$ (Figure 18b). As the unsteady circulation has the same dominant frequency as the spatial movement of the vortex near the ground, this supports our hypothesis that the unsteady separation from the ground may be responsible for the meandering.

3.4. Proper orthogonal decomposition analysis

The proper orthogonal decomposition (POD) analysis is a classical technique of probability theory, which expands a random function as a series of deterministic functions

with random coefficients so that it is possible to separate the deterministic part from the random one (Lumley 1970; Hinze 1975). The energy of stochastic signal is given by the sum of the eigenvalues so that each eigenvalue taken individually represents the energy contribution of the corresponding deterministic function (Berkooz et al. 1993). Lumley (1970) decomposed the velocity fields of turbulent flows as a spatial vectorial function and extracted the most energetic (spatial) eigenfunction representing the eddies of the flow. This analysis was applied to the trailing vortices from wings by Roy and Leweke (2008) and del Pino et al. (2011). In the present investigation of the inlet vortices, POD analysis was performed on the captured high frame-rate DPIV data at U_∞/U_i = 0.1 and 0.16. The analysis was performed using commercial software TSI GRAD-POD TOOLBOX, which employs the spatio-temporal data analysis technique proposed by Heiland (1992). For each case, the first 4 most energetic modes were extracted.

Figure 21 presents the relative energy distribution, time-averaged vorticity field and flow structures of dominant modes in the horizontal plane underneath the inlet for U_∞/U_i = 0.1. It can be observed that the 1st (most energetic) mode was centred on the time-averaged inlet vortex, contributing 30% of the total energy. It has an azimuthal symmetry of order 1, with the main direction parallel to the crosswind direction, representing a displacement of the vortex (Fabre et al. 2006). The 2nd mode (2nd energetic, contributing 5% of the total energy) was also centered on the time-averaged inlet vortex and has an azimuthal symmetry of order 1 with its main direction perpendicular to the crosswind. Hence, a linear combination of these eigenmodes provides displacements of the vortex core, which can be characterized as an azimuthal wavenumber of m = 1. It is interesting that Roy and Leweke (2008) and del Pino et al. (2011) found the same first helical mode in the POD analysis of the meandering of the trailing vortices from wings. Higher modes are also shown in Fig. 21, which indicates that the relative energy contributions of the 3rd and 4th modes are much smaller than those of the 1st

and 2nd modes. In fact, for all cases, the relative energy distribution was similar to that shown in Fig. 21. For a higher crosswind velocity of U_∞/U_i = 0.16 in this measurement plane (not shown here), observations were similar to those of U_∞/U_i = 0.1.

Time-averaged vorticity fields and the first (most energetic) mode flow structures of the results of POD analysis on the PIV data captured in the vertical plane at the inlet entrance and in the horizontal plane near the ground plane surface at U_∞/U_i = 0.1 and 0.16 are presented in Figures 22 and 23, respectively. The first modes in Figures 22 and 23 exhibit similar flow structures to those observed in the horizontal plane underneath the inlet (Fig. 21), i.e., centered on the time-averaged inlet vortex with an azimuthal symmetry of order 1. Figure 23 shows the main direction of the first mode to be parallel to the crosswind direction. These results suggest that the inlet vortex meander was dominated by a helical displacement wave m = 1.

Note that, for U_∞/U_i = 0.1, Figure 21 shows that flow structures of the 2nd mode have an azimuthal symmetry of order 1 but its main direction has an angle of 90° to the 1st mode. Similar results were also obtained at U_∞/U_i = 0.16. Since the 1st mode of the flow has a much larger energy contribution than the 2nd mode, the present POD analysis is consistent with the aforementioned discussion that the vortex meander was dominant in the direction of the crosswind in the horizontal plane underneath the inlet. For both crosswind velocities of U_∞/U_i = 0.1 and 0.16, similar results of POD analysis were also found in the horizontal plane near the ground plate surface and at the inlet entrance (not shown). These results are consistent with previous observations of an elliptical area of meandering.

4. Conclusions

The unsteady characteristics of inlet (ground) vortices have been investigated in a wind tunnel using a high-frame-rate digital particle image velocimetry system. The following conclusions can be drawn:

(1) When there is no wind, a pair of counter rotating inlet vortices exists, while for $U_\infty/U_i \neq 0$, only a single anti-clockwise vortex is formed. Near ground surface flow measurements indicate that the inlet vortex originates from the focus of separation formed on the ground. For a higher crosswind velocity of $U_\infty/U_i = 0.19$, the 'tornado' like vortex bends around the inlet due to the relatively strong crosswind, and does not enter into the inlet.

(2) Meandering was found in all measurement planes from near the ground to the inlet. The vortex meander is dominant in the direction of the crosswind and its amplitude increases with crosswind velocity.

(3) The time histories of the instantaneous vortex location exhibit quasi-periodic nature with dominant frequencies on the order of $fD_i/U_i = O(10^{-3})$ to $O(10^{-2})$. It was found that the meandering occurs at very large wavelengths. The present results also suggest that the unsteady characteristics of the focus of separation formed on the ground plane might be responsible for the inlet vortex dynamic behavior.

(4) The proper orthogonal decomposition (POD) analysis of the captured high frame-rate velocity data indicates that, for all cases, the most energetic mode was the first helical mode, representing a displacement of the vortex core.

Acknowledgments

The authors would like to thank the RCUK Academic Fellowship and also the EPSRC Engineering Instrument Pool of the United Kingdom.

References

Antkowiak, A. and Brancher, P., 2004, "Transient energy growth for the Lamb-Oseen vortex," *Physics of Fluids,* vol. 16, no. 1, pp. L1-L4.

Bailey, S. C. C. and Tavoularis, S., 2008, "Measurements of the velocity field of a wing-tip vortex, wandering in grid turbulence," *Journal of Fluid Mechanics,* vol. 601, pp. 281-315.

Bailey, S. C. C., Tavoularis, S. and Lee, B. H. K., 2006, "Effects of freestream turbulence on wing-tip vortex formulation and near field," *Journal of Aircraft*, vol. 43, No. 5, pp. 1282 – 1291.

Baker, G.R., Barker, S.J., Bofah, K.K. and Saffman, P.G., 1974, "Laser anemometer measurements of trailing vortices in water," *Journal of Fluid Mechanics,* vol. 65, pp. 325-336.

Beresh, S.J., Henfling, J.F. and Spillers, R.W., 2010, "Meander of a fin trailing vortex and the origin of its turbulence," *Experiments in Fluids*, vol. 49, No. 3, pp. 599 – 611.

Berkooz, Z., Holmes, P. and Lumley, J. L., 1993, "The proper orthogonal decomposition in the analysis of turbulent flows," *Annual Review of Fluid Mechanics*, vol. 25, pp. 539-575.

Brix, S., Neuwerth, G. and Jacob, D., 2000, "The inlet-vortex system of jet engines operating near the ground," *18th Applied Aerodynamics Conference*, 14-17 August, Denver, CO. AIAA 2000-3998.

Colehour, J. L. and Farquhar, B. W., 1971, "Inlet vortex," *Journal of Aircraft*, vol. 8, No. 1, pp. 39-43.

Corsiglia, V. R., Schwind, R. G. and Chigier, N. A., 1973, "Rapid scanning, three-dimensional hot-wire anemometer surveys of wing-tip vortices," *Journal of Aircraft*, vol. 10, No. 12, pp. 752 – 757.

De Siervi, F., Viguier, H. C., Greitzer, E. M. and Tan, C. S., 1982, "Mechanisms of inlet vortex formation," *Journal of Fluid Mechanics*, vol. 124, pp. 173-207.

Del Pino, C., Lopez-Alonso, J.M., Parras, L. and Fernandez-Feria, R., 2011, "Dynamics of the wing-tip vortex in the near field of a NACA 0012 airfoil," *The Aeronautical Journal,* vol. 115, No. 1166, pp. 229-239.

Devenport, W. J., Rife, M. C., Liapis, S. I. and Follin, G. J., 1996, "The structure and development of a wing-tip vortex," *Journal of Fluid Mechanics*, vol. 312, pp. 67 – 106.

Fabre, D., Sipp, D. and Jacquin, L., 2006, "Kelvin waves and the singular modes of the Lamb-Oseen vortex," *Journal of Fluid Mechanics*, vol. 551, pp. 235 – 274.

Funk, R., Parekh, D., Smith, D. and Dorris, J., 2001, "Inlet vortex alleviation," *19th AIAA Applied Aerodynamics conference*, 11-14 June, Anaheim, California. AIAA 2001-2449.

Gajewski, T., 1988, "Damping of the inlet vortex in a turbojet engine," *Journal of Technical Physics*, vol. 29, No. 3-4, pp. 337-348.

Green, S. I. and Acosta, A. J., 1991, "Unsteady flow in trailing vortices," *Journal of Fluid Mechanics*, vol. 227, pp. 107 – 173.

Gursul, I. and Xie, W., 2000, "Origin of vortex wandering over delta wings," *Journal of Aircraft,* vol. 37, no. 2, pp. 348-350.

Heiland, R. W., 1992, "*KLTOOL: A Mathematical Tool for Analyzing Spatiotemporal Data,'* Arizona State University, Dept of Mathematics, December.

Hinze, J. O., 1975, "*Turbulence,*" McGraw Hill, New York, second edition.

Jacquin, L., Fabre D, Geffroy, P. and Coustols, E., 2001, "The properities of a transport aircraft wake in the extended near field: an experimental study," 39th *AIAA Aerospace Sciences Meeting and Exhibit*, 8 - 11 January, Reno, NV. AIAA 2001-1038.

Jacquin, L., Fabre, D., Sipp, D., Theofilis, V. and Vollmers, H., 2003, "Instability and unsteadiness of aircraft wake vortices," *Aerospace Science and Technology,* vol. 7, pp. 577-593.

Johns, C. J., 2002, "The aircraft engine inlet vortex problem," *AIAA's Aircraft Technology, Integration, and Operations (ATIO) 2002 Technical*, 1-3 October, Los Angeles, California. AIAA 2002-5894.

Karlsson, A. and Fuchs, L., 2000, "Vortex systems and the interaction between an air inlet and the ground," ICAS 2000 Congress, pp. 522.1 – 522.10.

Klein, H.J., 1959, U.S. Patent for "Vortex inhibitor for aircraft jet engines," Douglas Aircraft Co., No. 2,915,262. B64D33/02, filed 1 December.

Leibovich, S., 1984, "Vortex stability and breakdown: Survey and extension," *AIAA Journal*, vol. 22, No. 9, pp. 1192 – 1206.

Lumley, J. L., 1970, "Stochastic Tools in Turbulence," *Applied Mathematics and Mechanics*, Vol. 12, Academic Press, New York.

Margaris, P., Marles, D. and Gursul, I., 2008, "Experiments on jet/vortex interaction," *Experiments in Fluids,* vol. 44, pp. 261-278.

Menke, M. and Gursul, I., 1997, "Unsteady nature of leading edge vortices," *Physics of Fluids*, vol. 9, No. 10, pp. 2960 – 2966.

Moffat, R.J., 1982, "Contributions to the theory of single-sample uncertainty analysis," *Journal of Fluids Engineering*, vol. 104, No. 2, pp. 250-260.

Murphy, J.P. and MacManus, D.G., 2011a, "Ground vortex aerodynamics under crosswind conditions," *Experiments in Fluids,* vol. 50, pp. 109-124.

Murphy, J.P. and MacManus, D.G., 2011b, "Inlet ground vortex aerodynamics under headwind conditions," *Aerospace Science and Technology,* vol. 15, pp. 207-215.

Murphy, J.P., MacManus, D.G. and Sheaf, C. T., 2010, "Experimental investigation of intake ground vorticities during takeoff," *AIAA Journal,* vol. 48, No. 3, pp. 688-701.

Nakayama, A. and Jones J., 1999, "Correlation for formation of inlet vortex formation," *AIAA Journal*, vol. 37, No. 4, pp. 508-510.

Rodert, L. A. and Garrett, F. B., 1955, "Ingestion of foreign objects into turbine engines by vortices," TN 3330, Feb., NACA.

Roy, C. and Leweke, T., 2008, "Experiments on vortex meandering," FAR-Wake Technical Report AST4-CT-2005-012238, CNRS-IRPHE, also presented in International Workshop on Fundamental Issues related to Aircraft Trailing Wakes, 27-29 May 2008, Marseille, France.

Secareanu, A., Moroianu, D., Karlsson, A. and Fuchs, L., 2005, "Experimental and numerical study of ground vortex interaction in an air-intake," *43rd AIAA Aerospace Sciences Meeting and Exhibit*, 10-13 January, Reno, NV, United States. AIAA2005-1206.

Shin, H. W., Cheng, W. K., Greitzer, E. M. and Tan, C. S., 1986a, "Inlet vortex formation due to ambient vorticity intensification," *AIAA Journal*, vol. 24, No. 4, pp. 687-689.

Shin, H. W., Greitzer, E. M., Cheng, W. K., Tan, C. S., and Shippee, C.L., 1986b, "Circulation measurements and vortical structure in an inlet-vortex flow field" *Journal of Fluid Mechanics*, vol. 162, pp 463-487.

Shmilovich, A. and Yadlin, Y., 2006, "Engine ground vortex control," *24th Applied Aerodynamics Conference*, 5-8 June, San Francisco, California. AIAA2006-3006.

Trapp, L. G. and Girardi, R. M., 2010, "Crosswind effects on engine inlet: the inlet vortex," *Journal of Aircraft*, vol. 47, No. 2, pp. 577-590.

Tsai, C-Y. and Widnall, S.E., 1980, "Examination of group-velocity criterion for breakdown of vortex flow in a divergent duct", *Physics of Fluids,* vol. 23, no. 5, pp. 864-870.

Williams, N. M., 2009, "Active flow control on a nonslender delta wing," PhD Thesis, Mechanical Engineering (University of Bath).

List of Figures

Figure 10. Probability P of instantaneous inlet vortex locations near the ground surface. The black symbol indicates the time-averaged location. (a) $U_\infty/U_i = 0.1$; (b) $U_\infty/U_i = 0.16$; (c) $U_\infty/U_i = 0.19$. The schematic shows the measurement plane.

Figure 11. Variations of (a) the standard deviation SD of the coordinates of inlet vortex location in the crosswind and perpendicular to the crosswind directions, and (b) vortex meandering amplitude a_M, as a function of crosswind velocity.

Figure 12. Tangential velocity profiles across instantaneous and time-averaged vortex centres in the horizontal plane underneath inlet at $U_\infty/U_i = 0.16$. Here u and v are the velocity components in the directions of crosswind and perpendicular to crosswind, respectively.

Figure 13. Variation of conditionally-averaged radius of the instantaneous vortex, r_{oi}/D_i, as a function of crosswind velocity.

Figure 14. Variations of vortex meandering amplitude a_M normalized by the conditionally-averaged radius of instantaneous vortex as a function of crosswind velocity.

Figure 15. Time histories of the coordinates of inlet vortex location in the crosswind direction in the plane which is (a) parallel and close to the edge of the inlet at $y=-0.03D_i$, (b) near the ground plate surface at $z=-0.73D_i$. $U_\infty/U_i = 0.16$.

Figure 16. Frequency spectrum of the coordinates x_i/D_i of inlet vortex location in the crosswind direction in the plane which is (a) parallel and close to the edge of the inlet at $y=-0.03D_i$, (b) near the ground plate surface at $z=-0.73D_i$. $U_\infty/U_i = 0.16$.

Figure 17. Time histories of the coordinates of inlet vortex location in the crosswind direction in the plane which is (a) underneath the inlet and parallel to the ground plate at $z=-0.57D_i$, (b) near the ground plate surface at $z=-0.73D_i$. $U_\infty/U_i = 0.19$.

Figure 18. Frequency spectrum of the coordinates x_i/D_i of inlet vortex location in the crosswind direction in the plane which is (a) underneath the inlet and parallel to the ground plate at $z=-0.57D_i$, (b) near the ground plate surface at $z=-0.73D_i$. $U_\infty/U_i = 0.19$.

Figure 19. Frequency spectrum of the coordinates x_i of inlet vortex location in the crosswind direction in the plane which is (a) at inlet entrance; (b) in a plane underneath the inlet and parallel to the ground plate and (c) near the ground surface.

Figure 20. (a) Time history of the circulation of instantaneous inlet vortex, and (b) Frequency spectrum of the variation of circulation Γ of instantaneous inlet vortex near the ground plate surface at z = -0.73D_i. U_∞/U_i = 0.19.

Figure 21. Relative energy distribution, time-averaged vorticity field and flow structures of dominant modes in a plane underneath the inlet and parallel to the ground plate at z= -0.57D_i. U_∞/U_i = 0.1. Crosswind from right to left. The schematic shows the measurement plane.

Figure 22. Time-averaged vorticity fields and the first mode in the plane which is parallel and close to the edge of the inlet at y= -0.03D_i. (a) U_∞/U_i = 0.1; (b) U_∞/U_i = 0.16. Crosswind from right to left. The schematic shows the measurement plane.

Figure 23. Time-averaged vorticity fields and the first mode near the ground plate surface at z = -0.73D_i. (a) U_∞/U_i = 0.1; (b) U_∞/U_i = 0.16. Crosswind from right to left. The schematic shows the measurement plane.

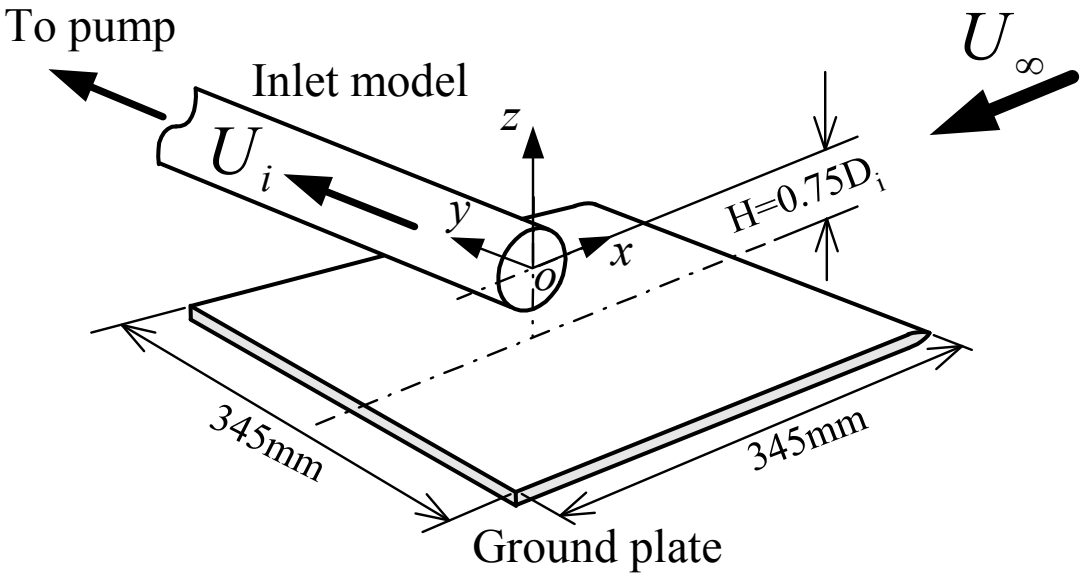

Figure 1. Experimental arrangement.

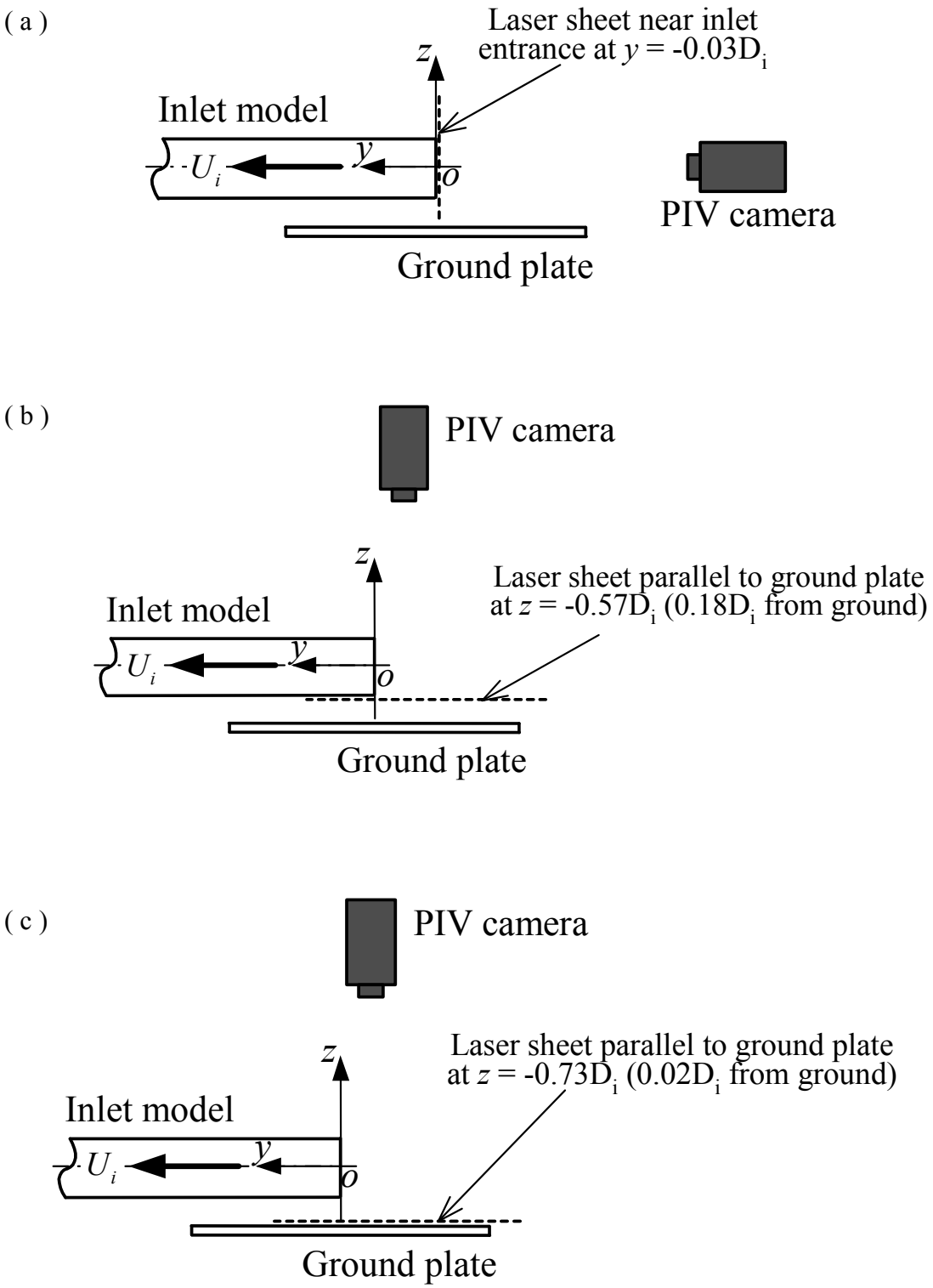

Figure 2. Schematic of PIV measurements for (a) in the vertical plane which is parallel and close to the edge of the inlet; (b) in a plane underneath the inlet and parallel to the ground plate and (c) near the ground surface.

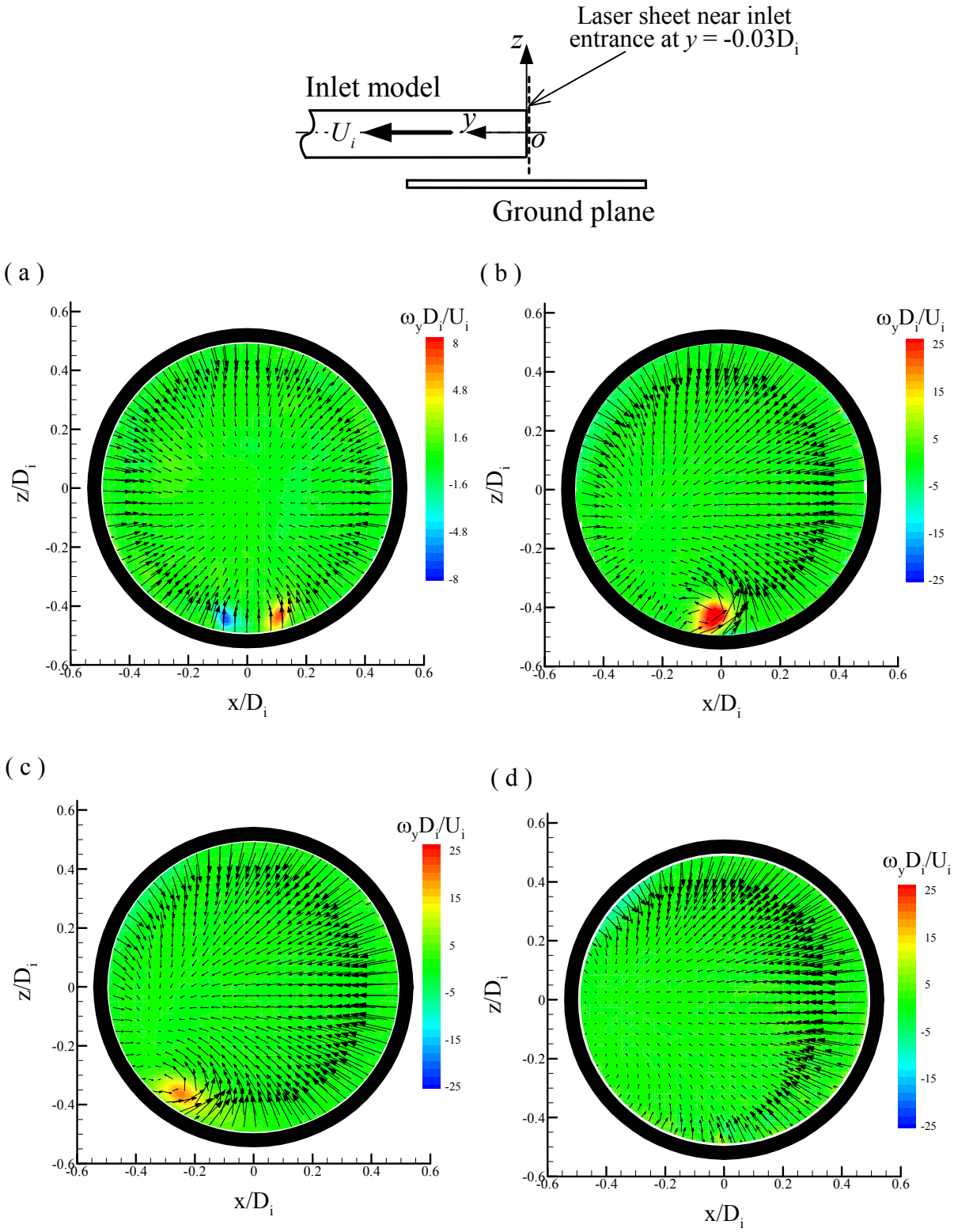

Figure 3. Time-averaged vorticity field in the plane which is parallel and close to the edge of the inlet at y=-0.03D$_i$. (a) U_∞/U_i = 0; (b) U_∞/U_i = 0.1; (c) U_∞/U_i = 0.16; (d) U_∞/U_i = 0.19. Crosswind from right to left. The schematic shows the measurement plane.

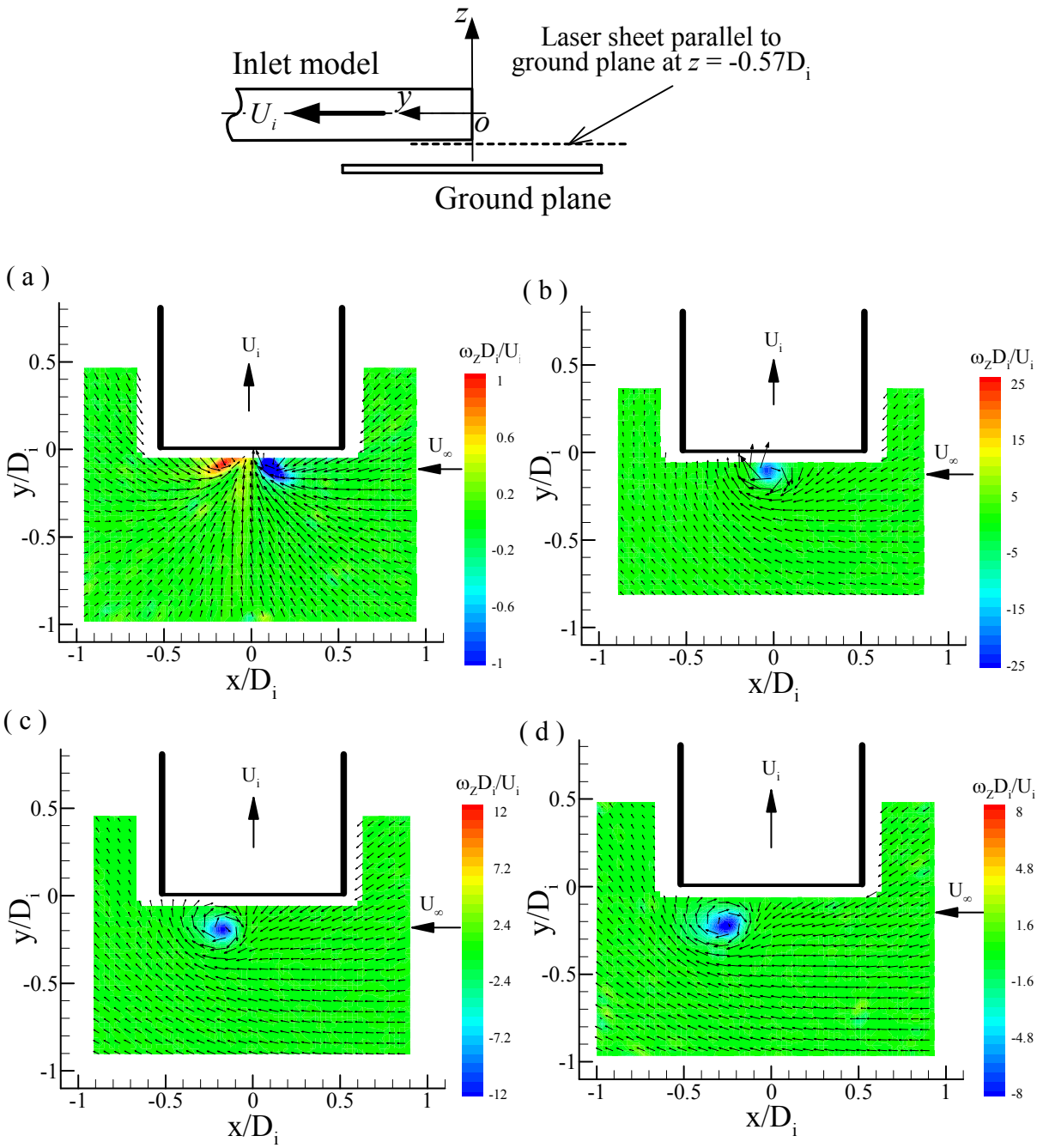

Figure 4. Time-averaged vorticity field in a plane underneath the inlet and parallel to the ground plate at z=-0.57D$_i$ (0.18D$_i$ from ground). (a) U_∞/U_i = 0; (b) U_∞/U_i = 0.1; (c) U_∞/U_i = 0.16; (d) U_∞/U_i = 0.19. Crosswind from right to left. The schematic shows the measurement plane.

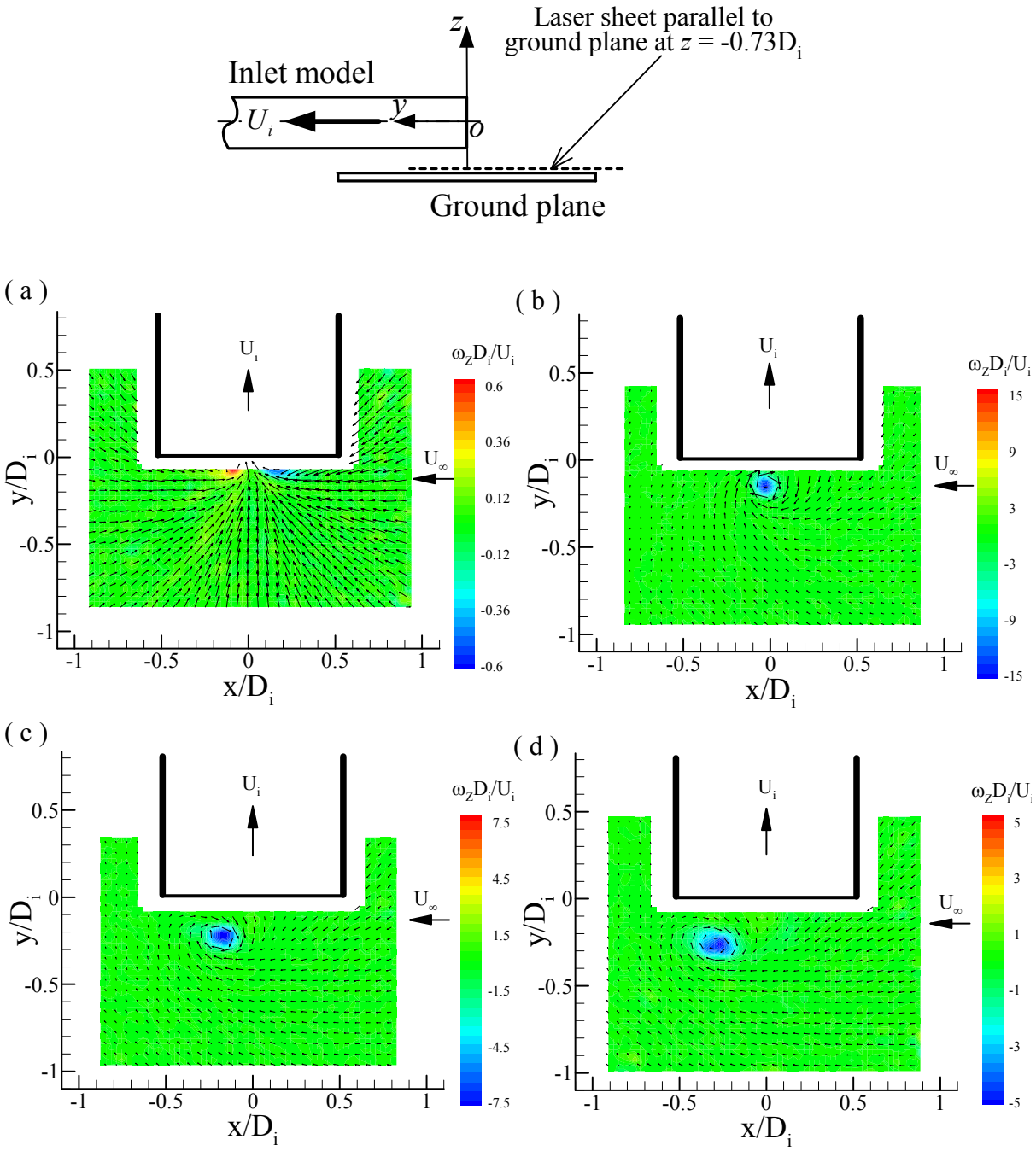

Figure 5. Time-averaged vorticity field near the ground surface at z = -0.73D$_i$ (0.02D$_i$ from ground). (a) U_∞/U_i = 0; (b) U_∞/U_i = 0.1; (c) U_∞/U_i = 0.16; (d) U_∞/U_i = 0.19. Crosswind from right to left. The schematic shows the measurement plane.

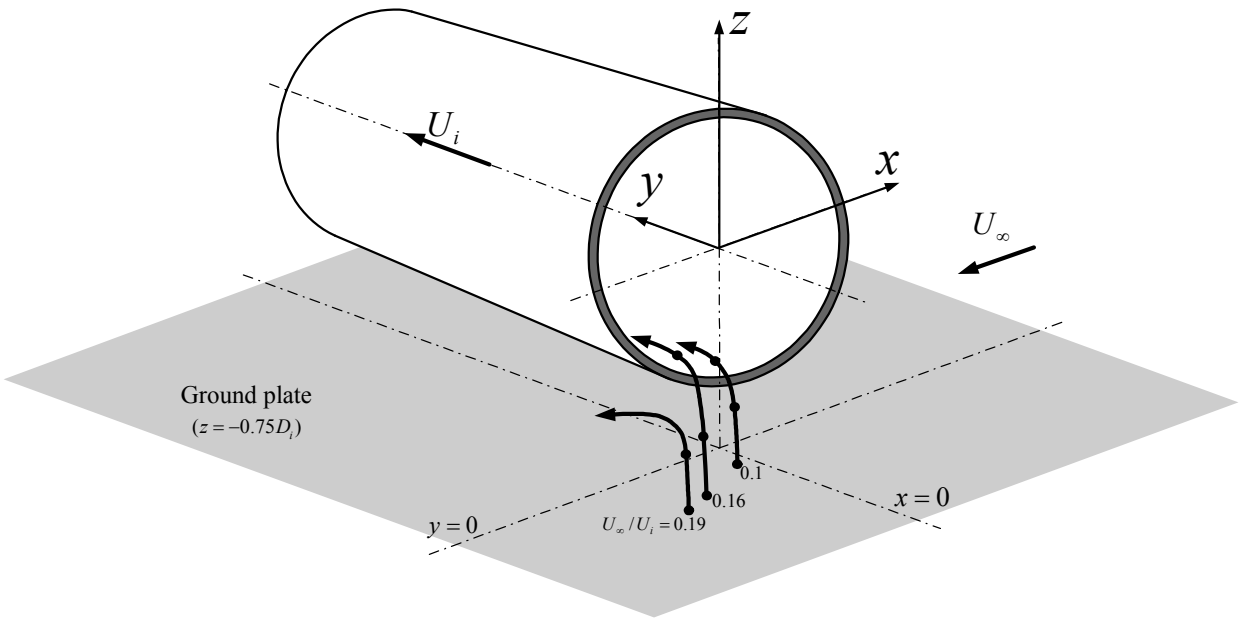

Figure 6. Vortex topology for different crosswind velocity ratios.

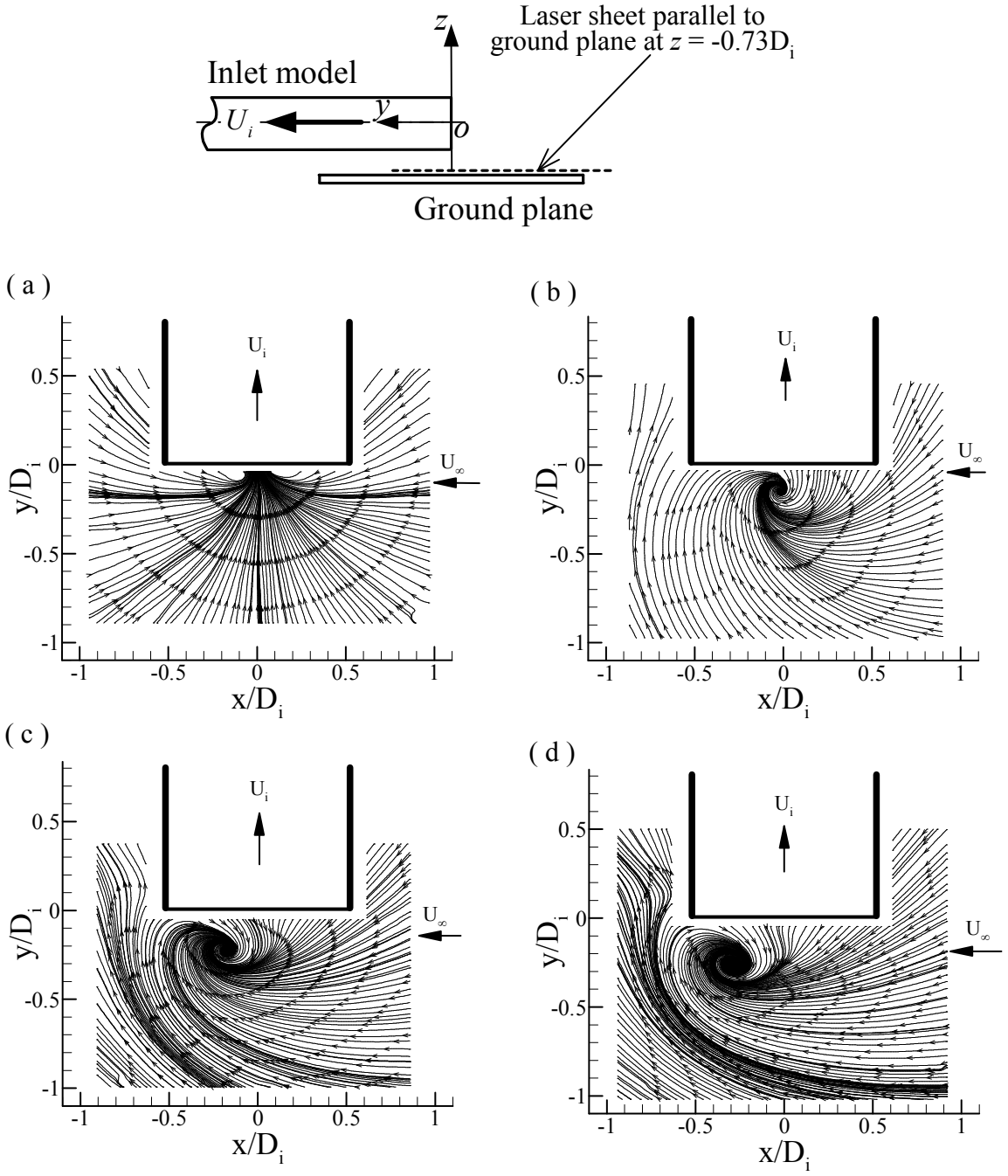

Figure 7. Time-averaged streamline patterns near the ground surface at z = -0.73D$_i$ (0.02D$_i$ from ground). (a) U_∞/U_i = 0; (b) U_∞/U_i = 0.1; (c) U_∞/U_i = 0.16; (d) U_∞/U_i = 0.19. Crosswind from right to left. The schematic shows the measurement plane.

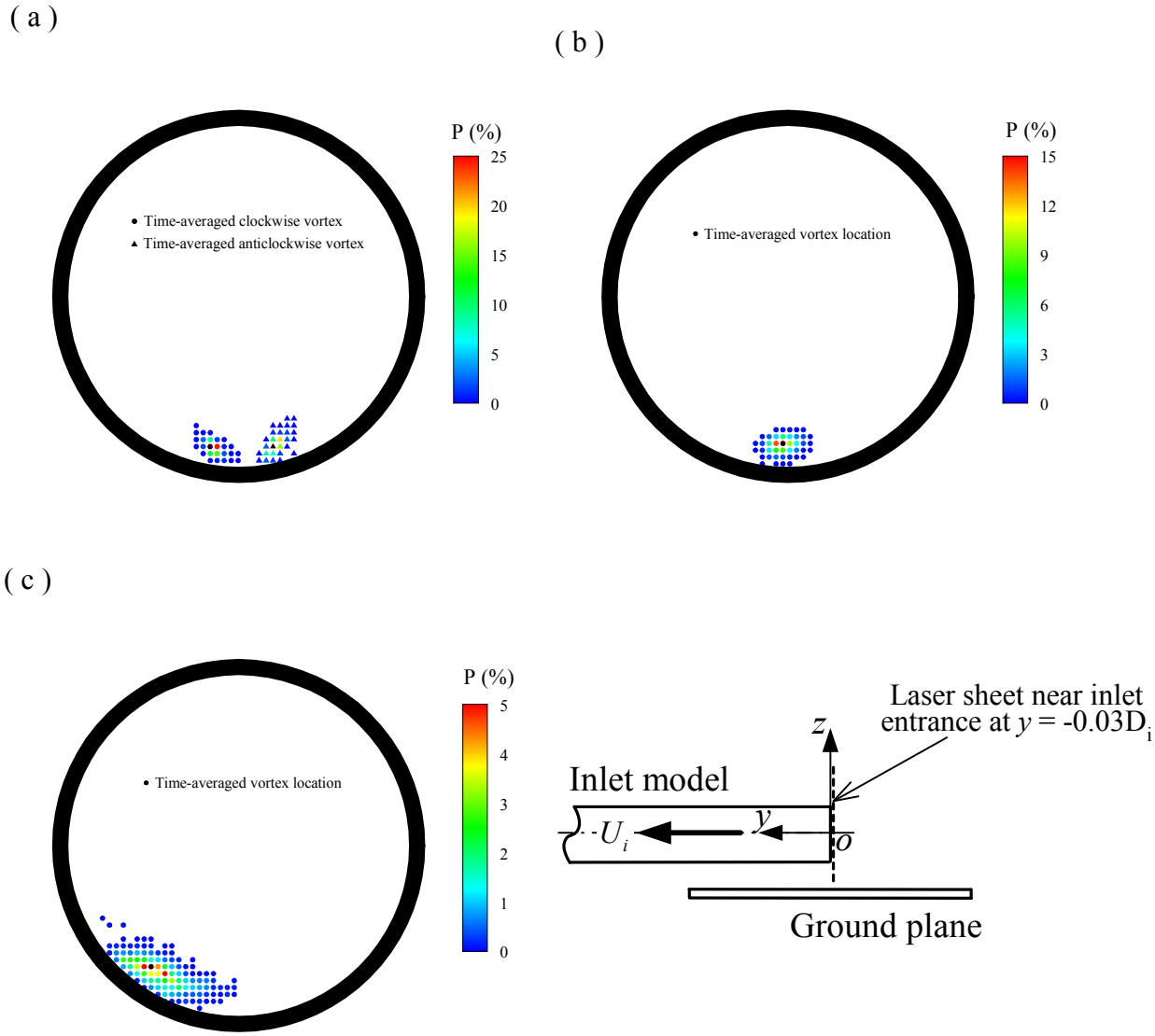

Figure 8. Probability P of instantaneous inlet vortex locations in the plane which is parallel and close to the edge of the inlet. The black symbol indicates the time-averaged location of inlet vortex. (a) $U_\infty/U_i = 0$; (b) $U_\infty/U_i = 0.1$; (c) $U_\infty/U_i = 0.16$. Crosswind from right to left. The schematic shows the measurement plane.

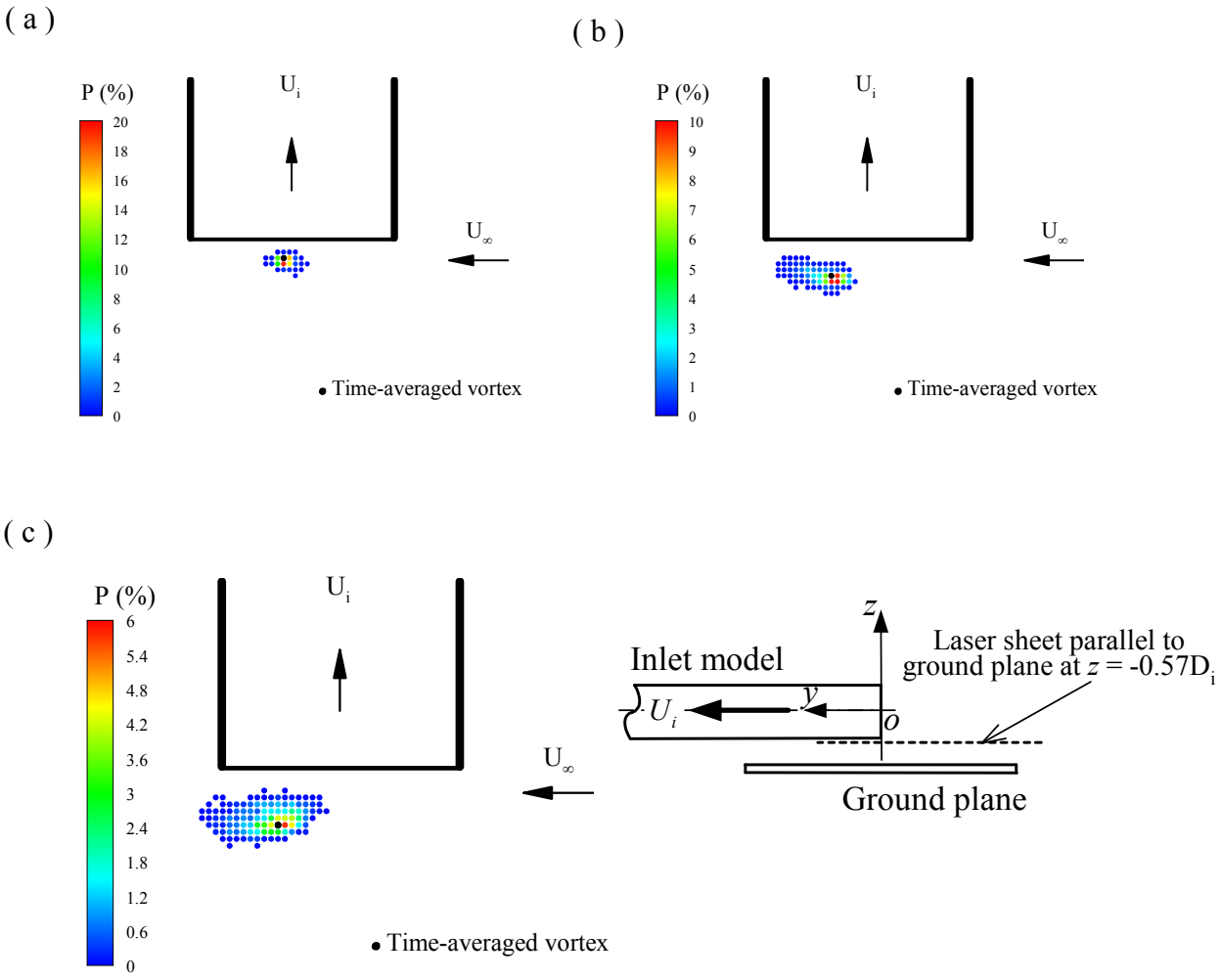

Figure 9. Probability P of instantaneous inlet vortex locations in the plane underneath the inlet and parallel to the ground plate. The black symbol indicates the time-averaged location of inlet vortex. (a) U_∞/U_i = 0.1; (b) U_∞/U_i = 0.16; (c) U_∞/U_i = 0.19. The schematic shows the measurement plane.

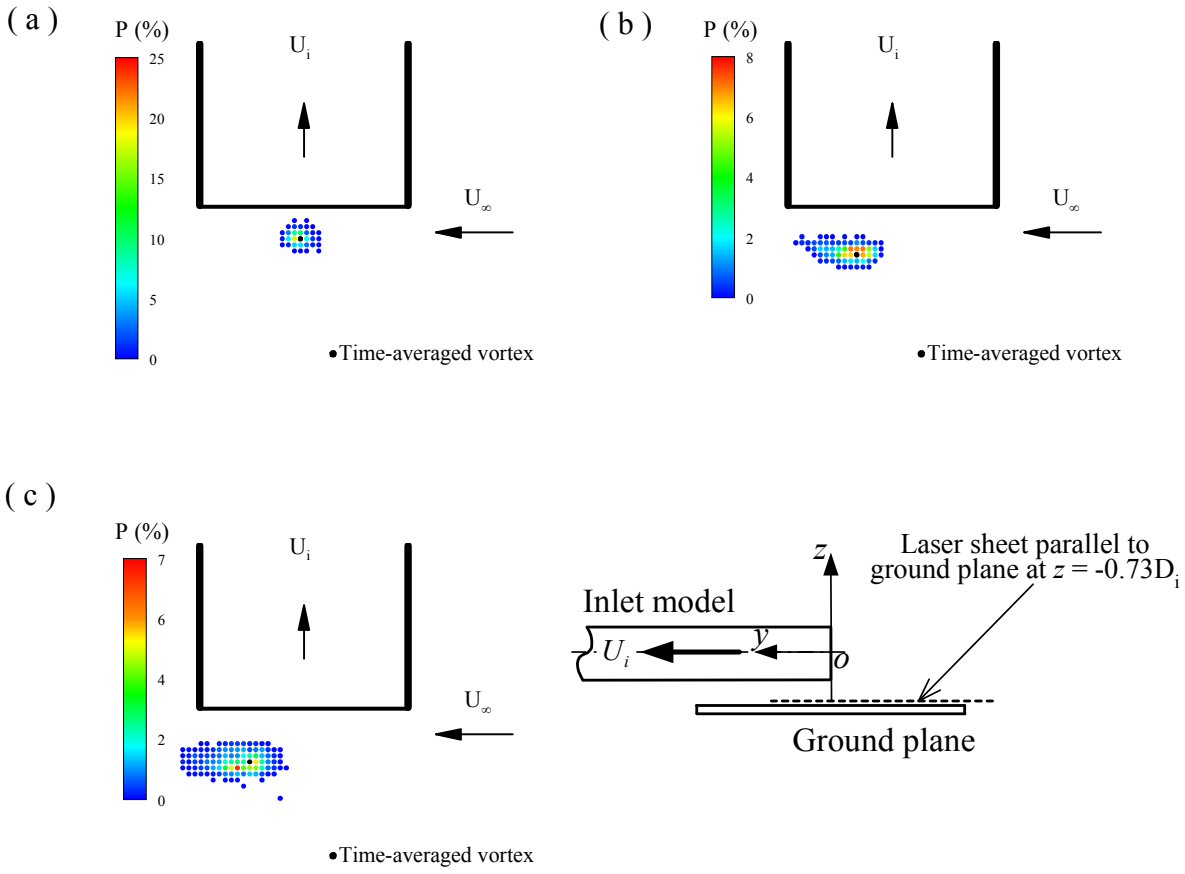

Figure 10. Probability P of instantaneous inlet vortex locations near the ground surface. The black symbol indicates the time-averaged location. (a) U_∞/U_i = 0.1; (b) U_∞/U_i = 0.16; (c) U_∞/U_i = 0.19. The schematic shows the measurement plane.

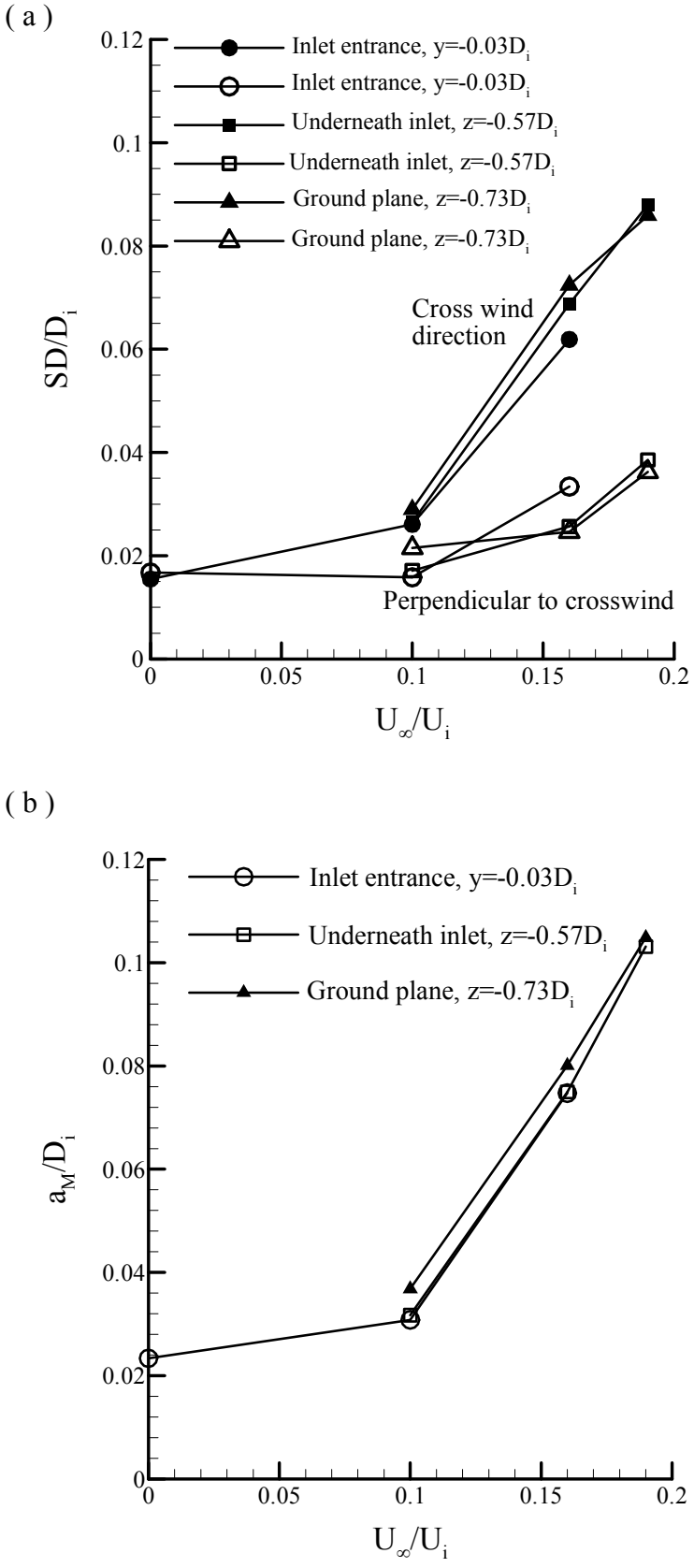

Figure 11. Variations of (a) the standard deviation SD of the coordinates of inlet vortex location in the crosswind and perpendicular to the crosswind directions, and (b) vortex meandering amplitude a_M, as a function of crosswind velocity.

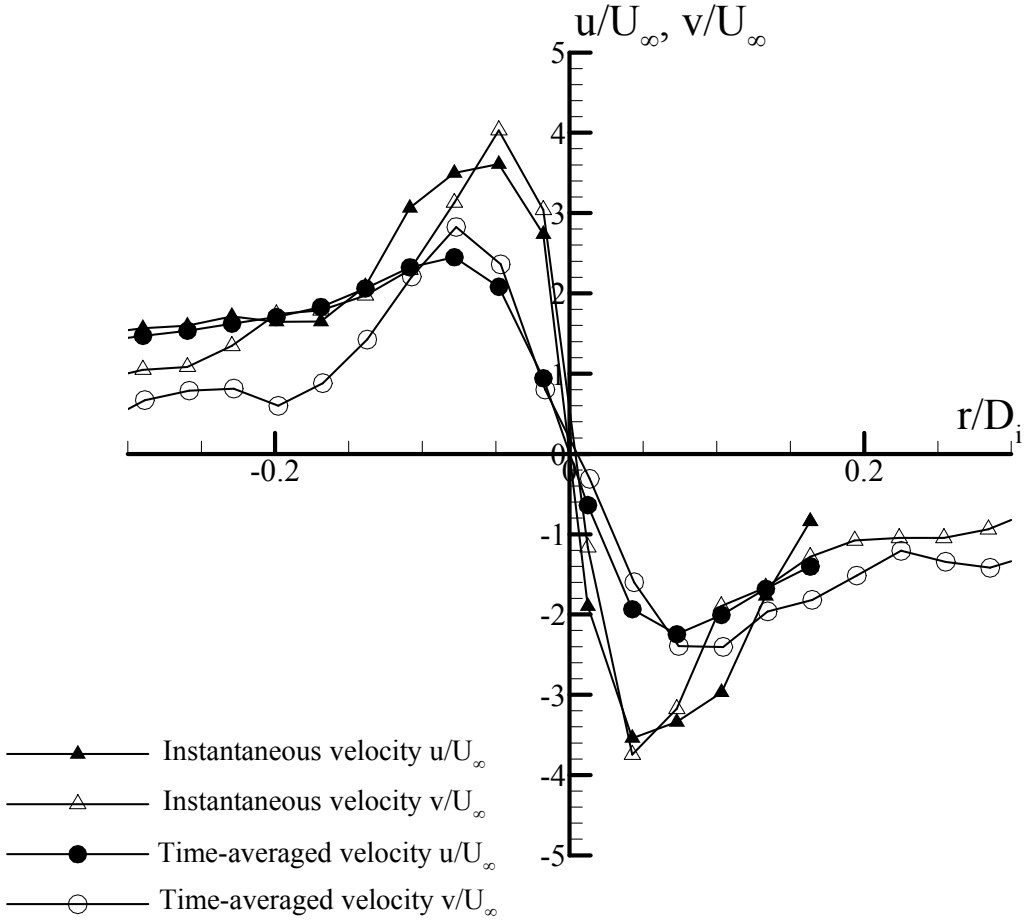

Figure 12. Tangential velocity profiles across instantaneous and time-averaged vortex centres in the horizontal plane underneath inlet at U_∞/U_i = 0.16. Here u and v are the velocity components in the directions of crosswind and perpendicular to crosswind, respectively.

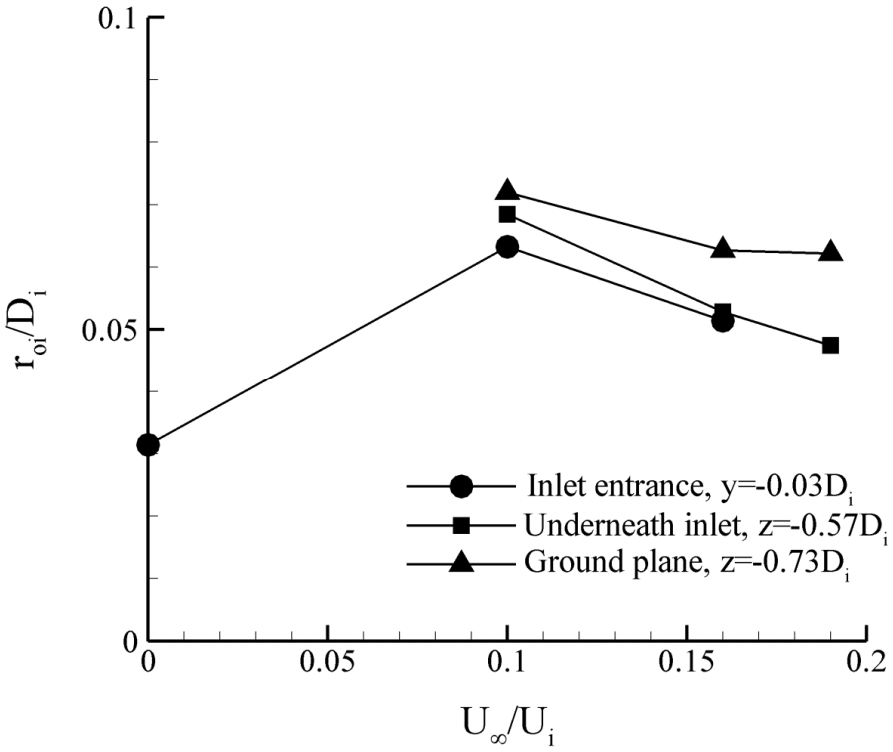

Figure 13. Variation of conditionally-averaged radius of the instantaneous vortex, r_{oi}/D_i, as a function of crosswind velocity.

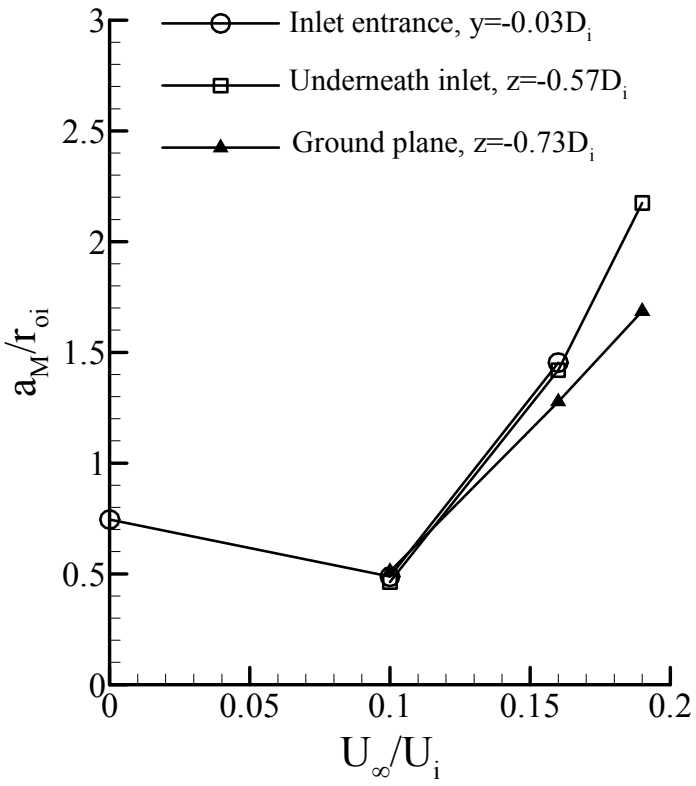

Figure 14. Variation of vortex meandering amplitude a_M normalized by the conditionally-averaged radius of instantaneous vortex as a function of crosswind velocity.

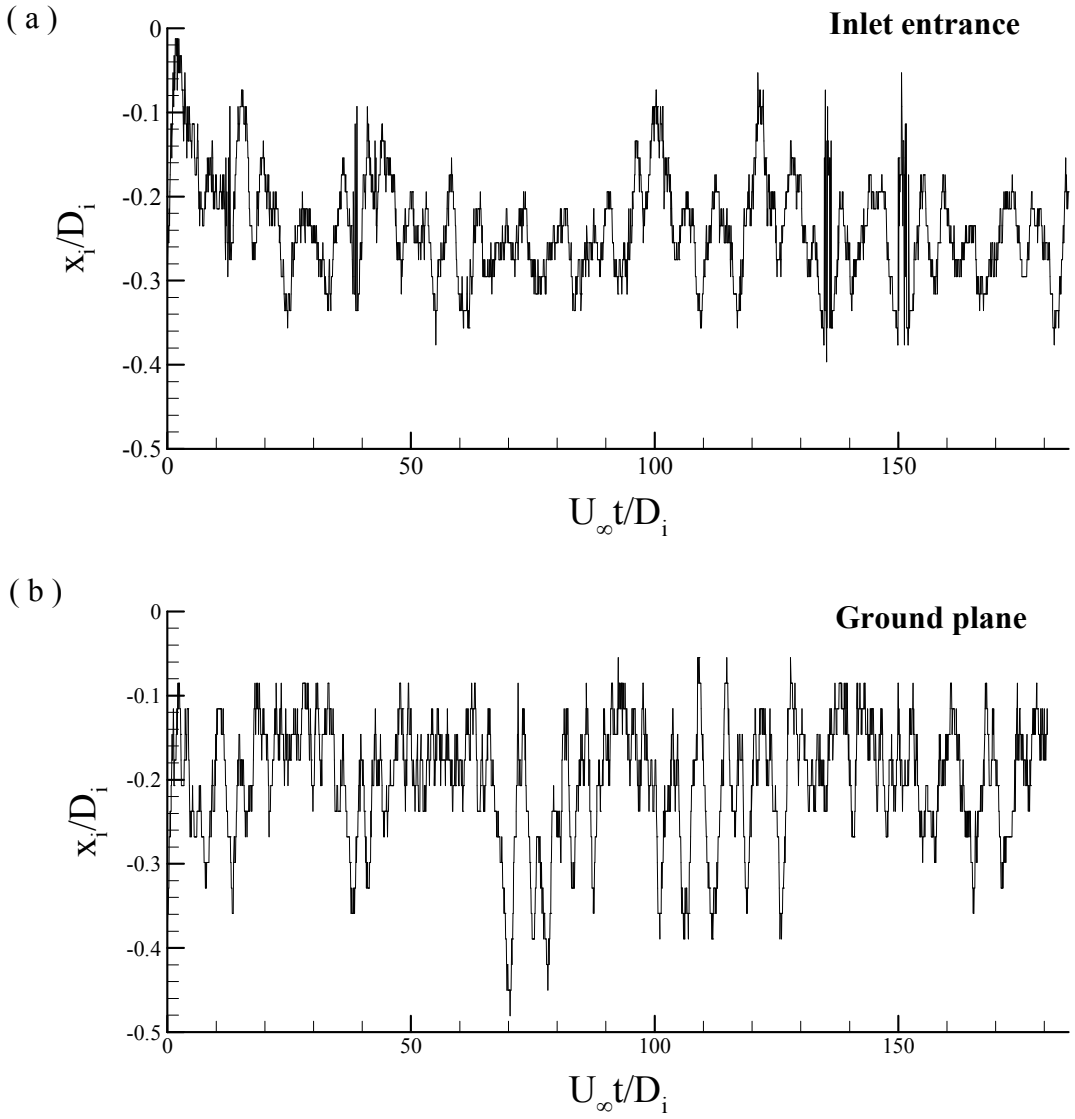

Figure 15. Time histories of the coordinates of inlet vortex location in the crosswind direction in the plane which is (a) parallel and close to the edge of the inlet at $y=-0.03D_i$, (b) near the ground plate surface at $z=-0.73D_i$. $U_\infty/U_i = 0.16$.

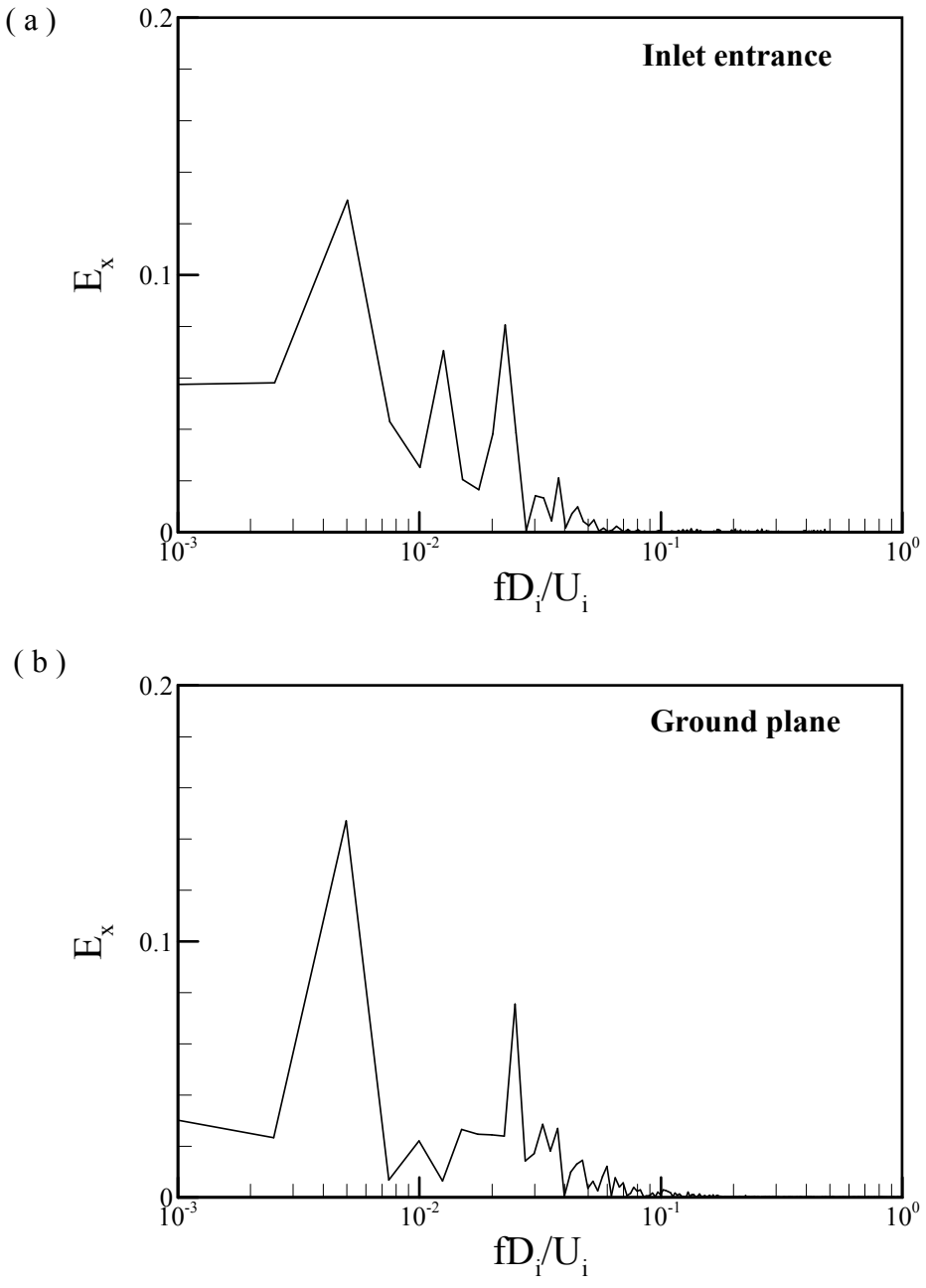

Figure 16. Frequency spectrum of the coordinates x_i/D_i of inlet vortex location in the crosswind direction in the plane which is (a) parallel and close to the edge of the inlet at $y=-0.03D_i$, (b) near the ground plate surface at $z=-0.73D_i$. $U_\infty/U_i = 0.16$.

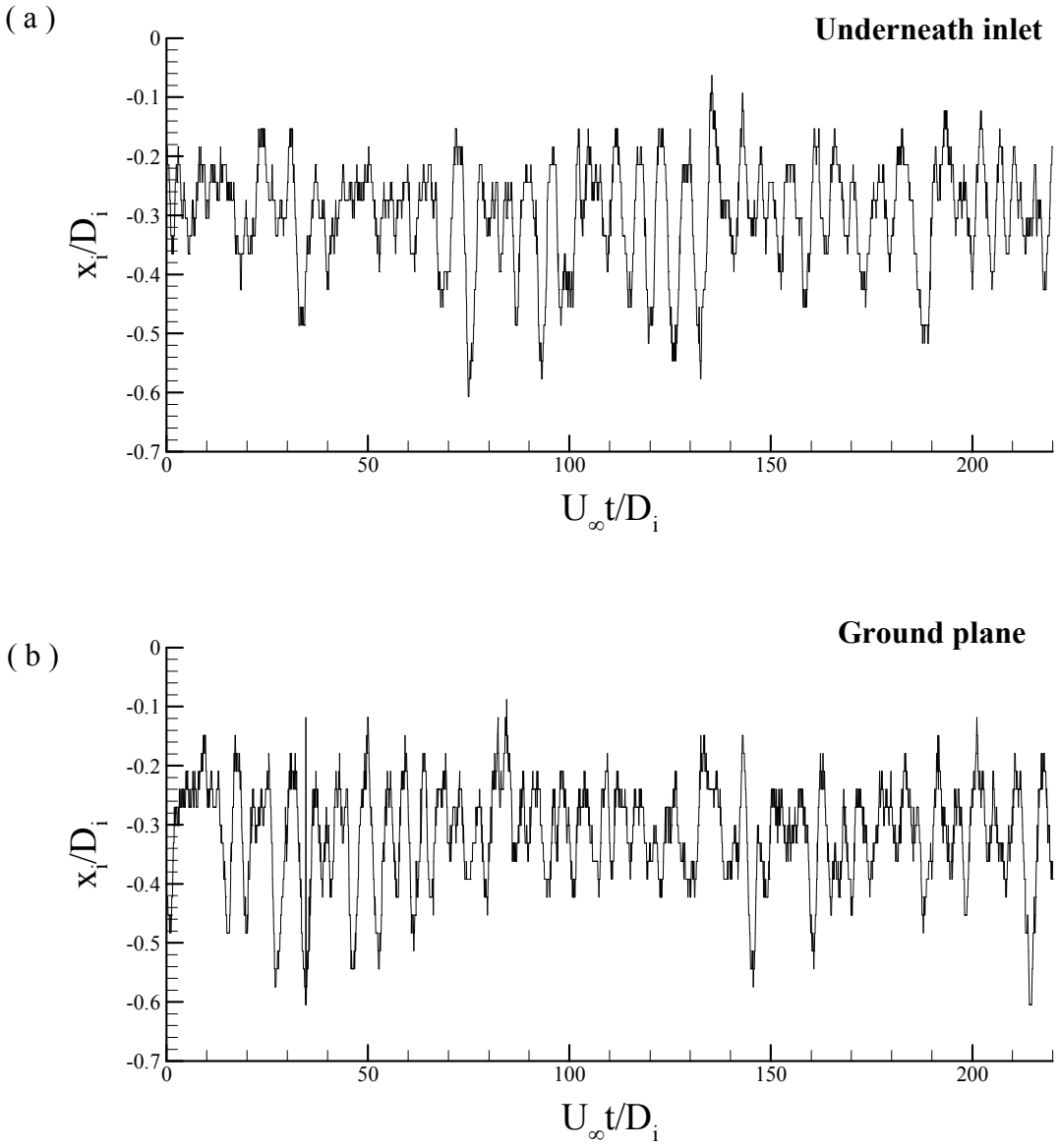

Figure 17. Time histories of the coordinates of inlet vortex location in the crosswind direction in the plane which is (a) underneath the inlet and parallel to the ground plate at $z=-0.57D_i$, (b) near the ground plate surface at $z=-0.73D_i$. $U_\infty/U_i = 0.19$.

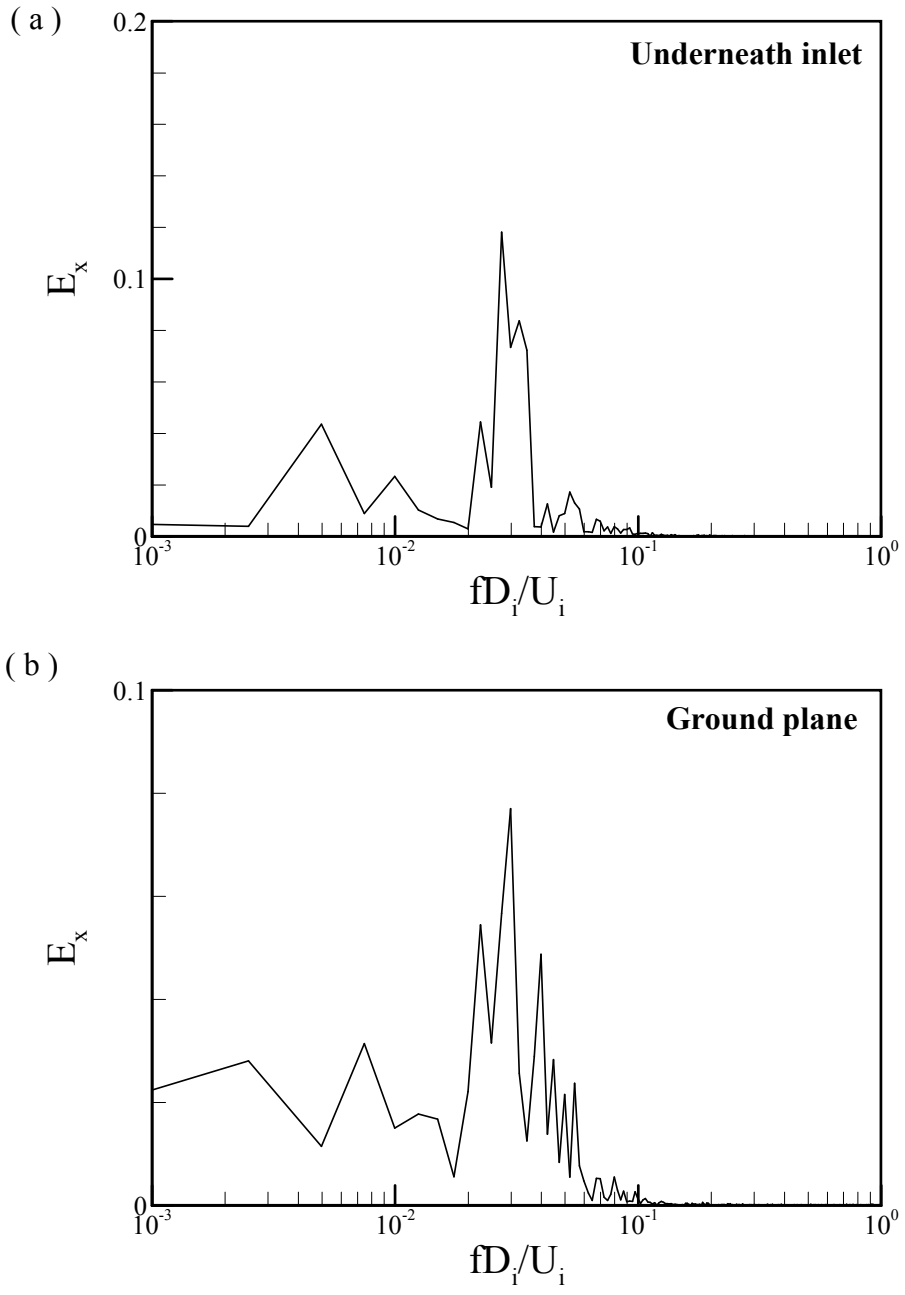

Figure 18. Frequency spectrum of the coordinates x_i/D_i of inlet vortex location in the crosswind direction in the plane which is (a) underneath the inlet and parallel to the ground plate at z=-0.57D$_i$, (b) near the ground plate surface at z=-0.73D$_i$. U_∞/U_i = 0.19.

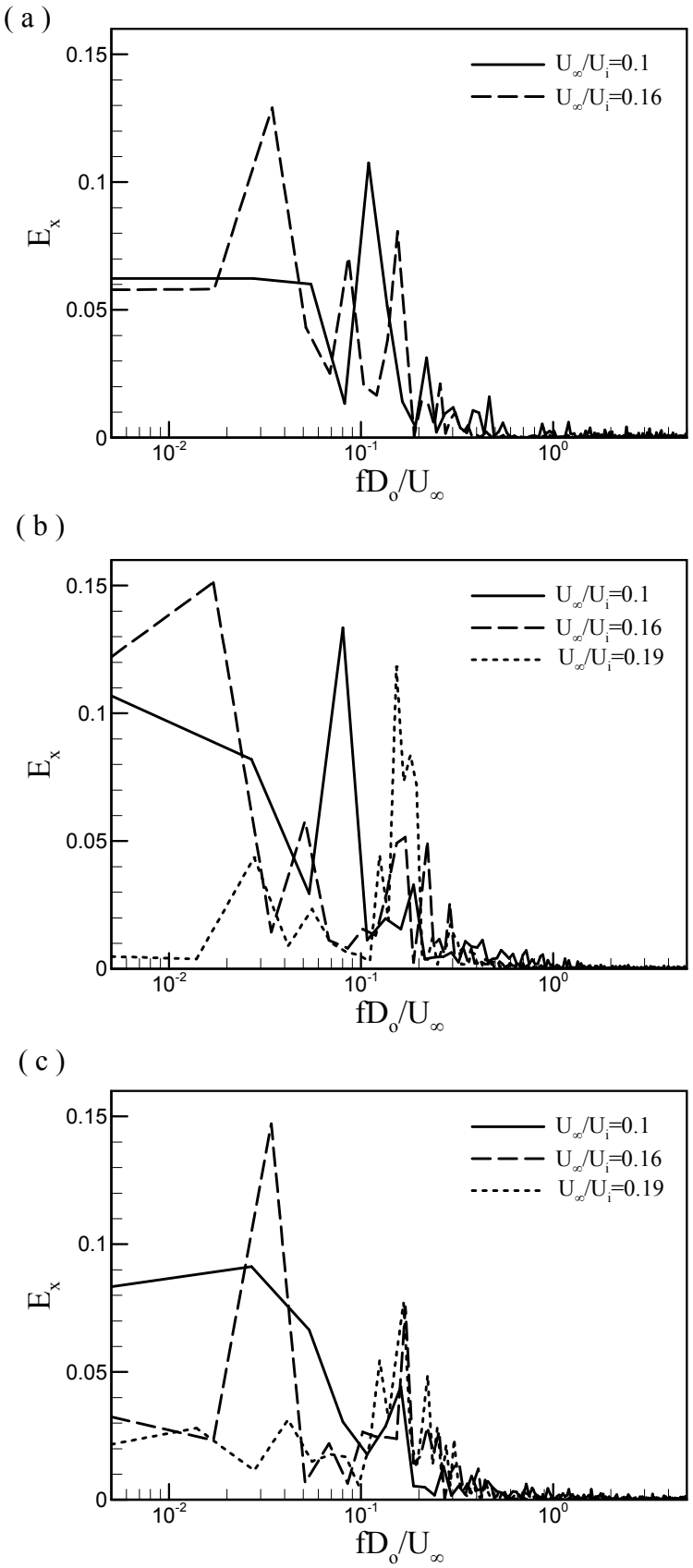

Figure 19. Frequency spectrum of the coordinates x_i of inlet vortex location in the crosswind direction in the plane which is (a) at inlet entrance; (b) in a plane underneath the inlet and parallel to the ground plate and (c) near the ground surface.

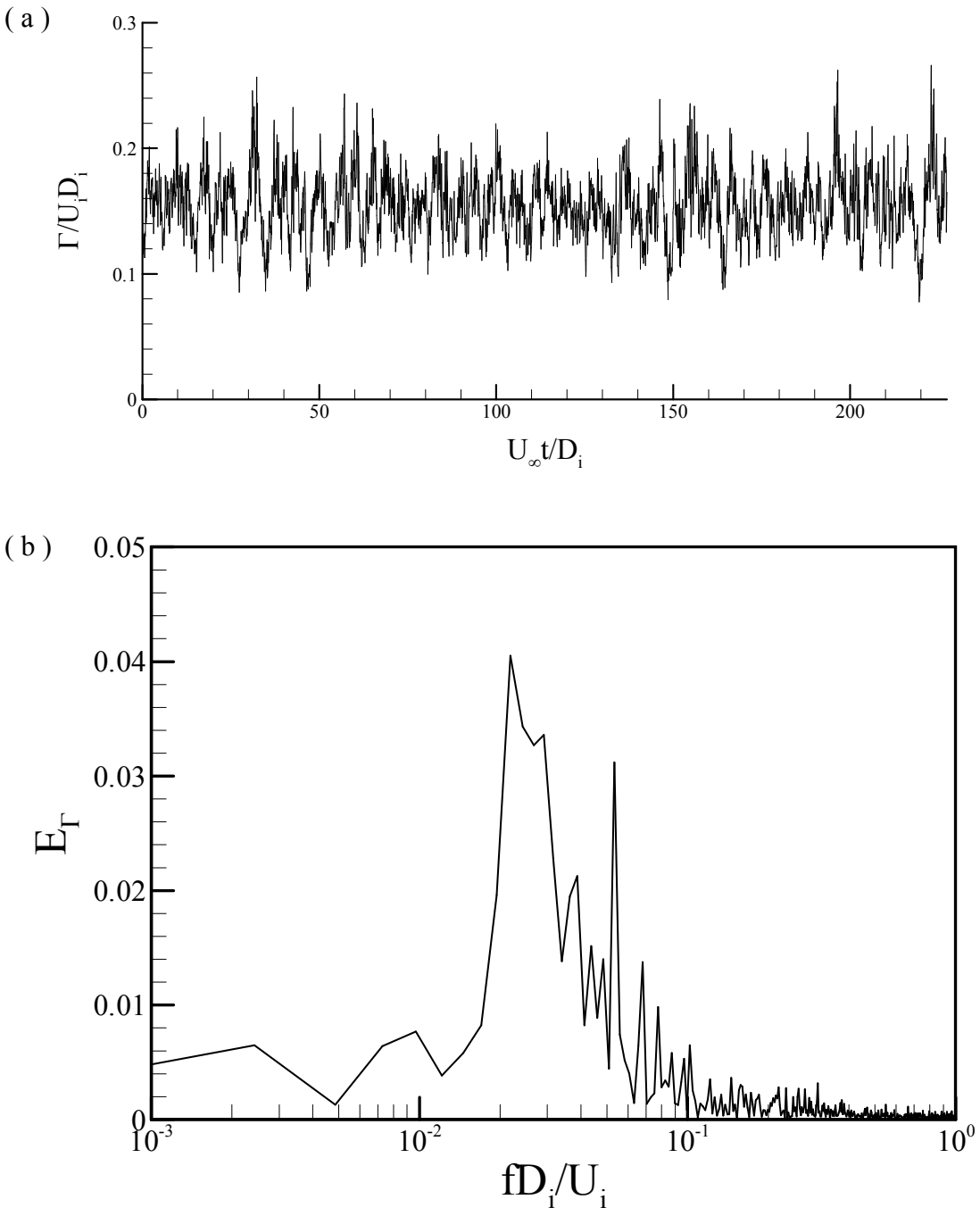

Figure 20. (a) Time history of the circulation of instantaneous inlet vortex, and (b) Frequency spectrum of the variation of circulation Γ of instantaneous inlet vortex near the ground plate surface at z = -0.73D$_i$. U_∞/U_i = 0.19.

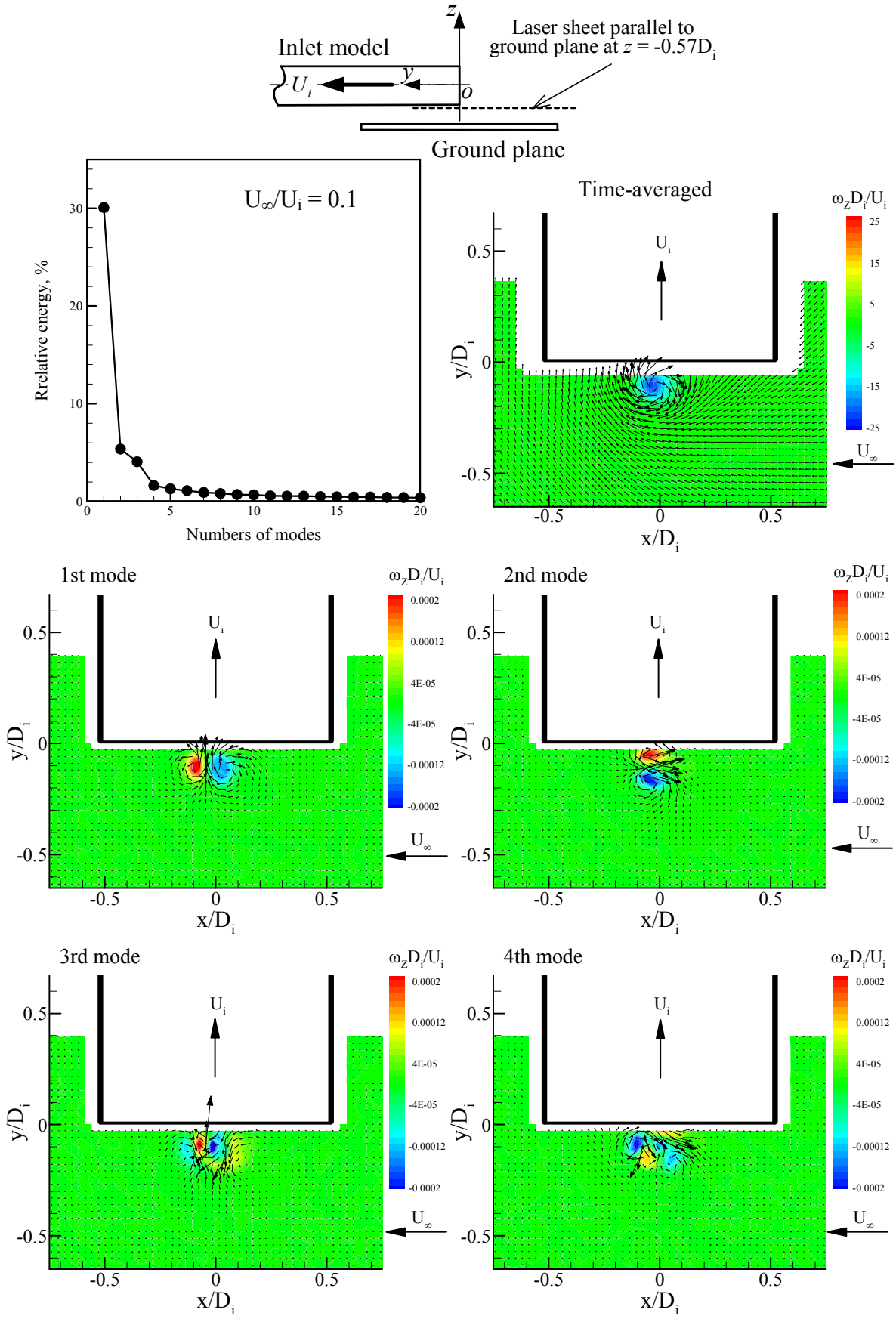

Figure 21. Relative energy distribution, time-averaged vorticity field and flow structures of dominant modes in a plane underneath the inlet and parallel to the ground plate at z= -0.57D$_i$. U_∞/U_i = 0.1. Crosswind from right to left. The schematic shows the measurement plane.

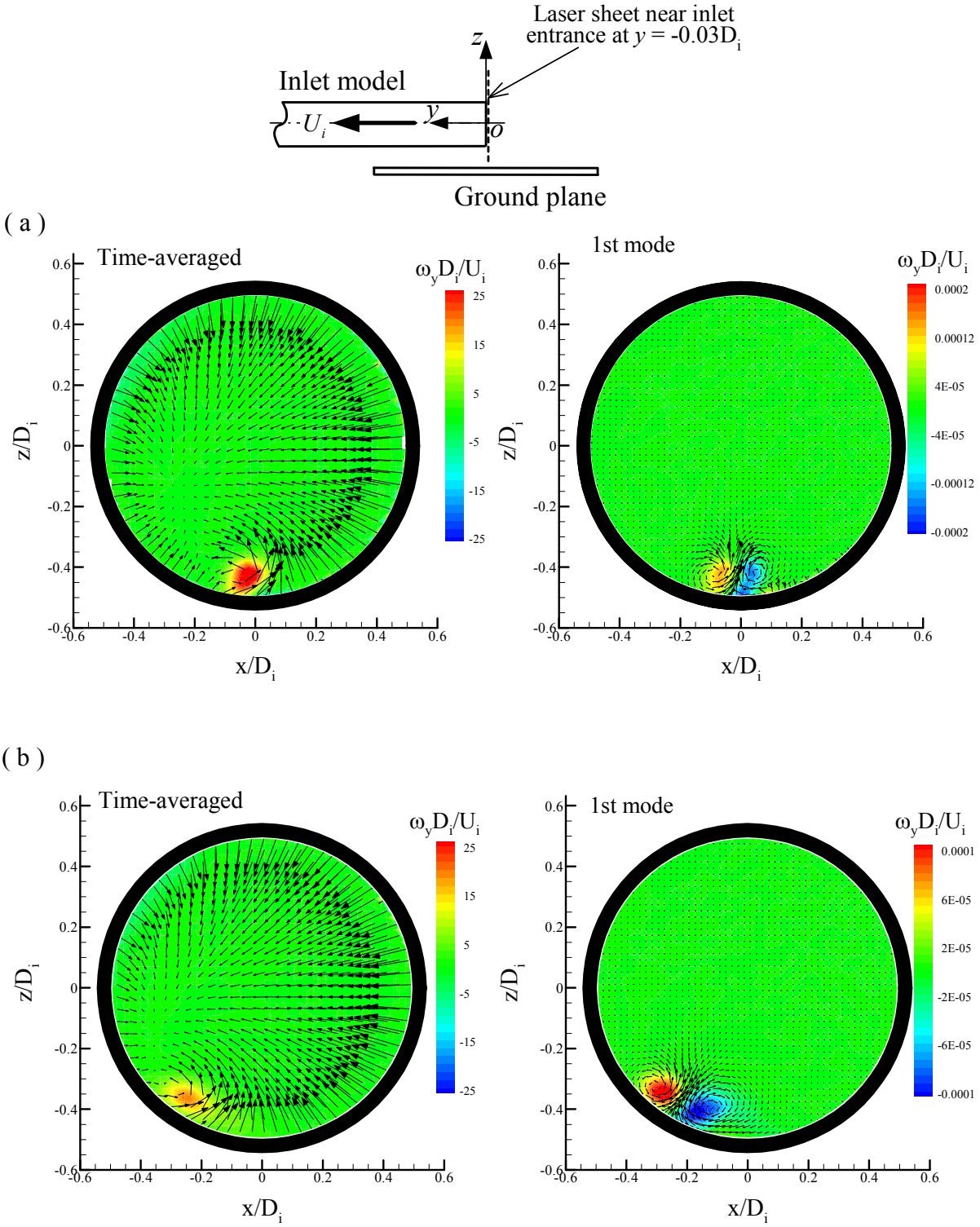

Figure 22. Time-averaged vorticity fields and the first mode in the plane which is parallel and close to the edge of the inlet at y= -0.03D$_i$. (a) U_∞/U_i = 0.1; (b) U_∞/U_i = 0.16. Crosswind from right to left. The schematic shows the measurement plane.

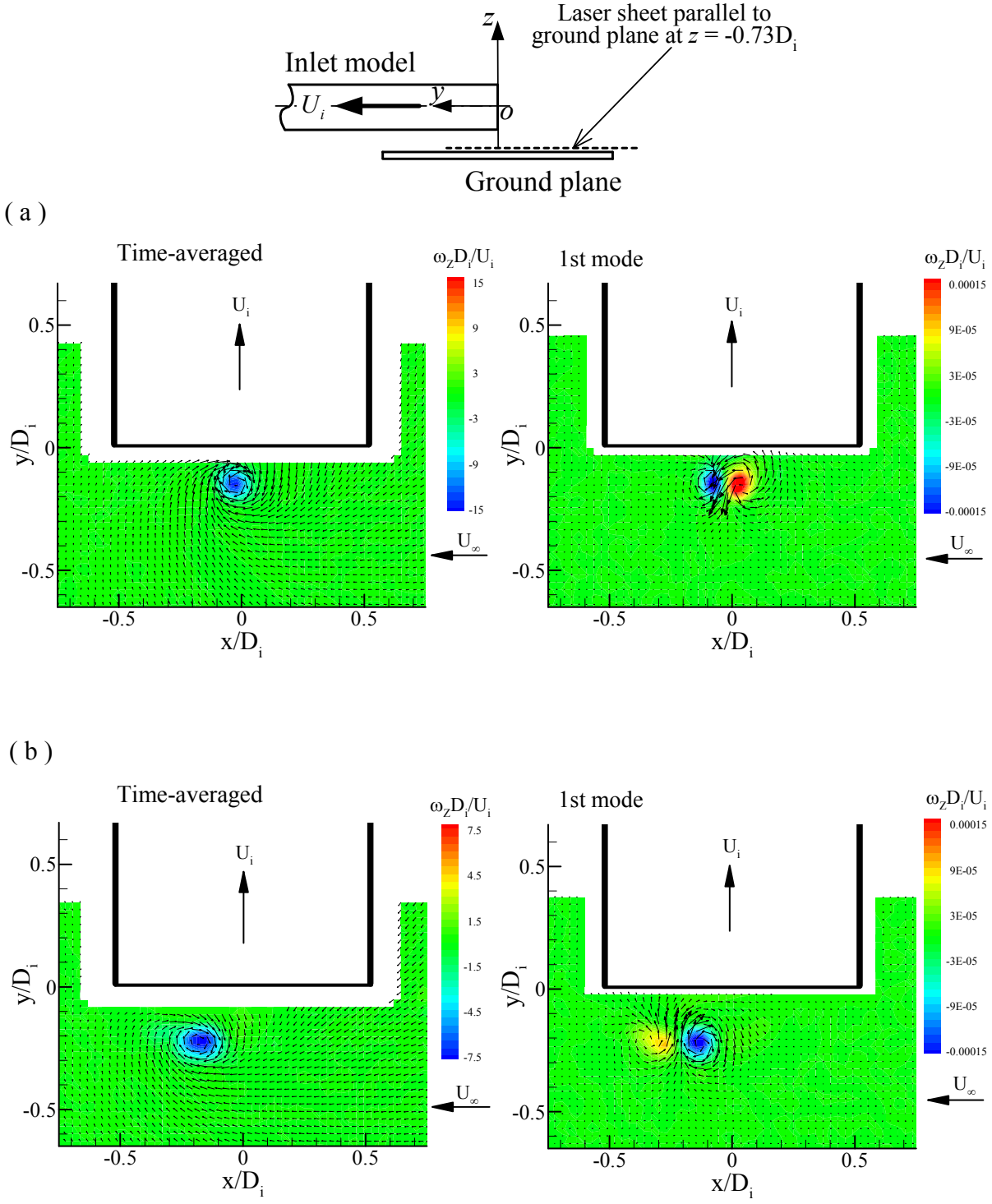

Figure 23. Time-averaged vorticity fields and the first mode near the ground plate surface at z = -0.73D$_i$. (a) U_∞/U_i = 0.1; (b) U_∞/U_i = 0.16. Crosswind from right to left. The schematic shows the measurement plane.